Lithos 380–381 (2021) 105833

Contents lists available at ScienceDirect

Lithos

journal homepage: www.elsevier.com/locate/lithos

Research Article

Early Paleozoic magmatic "flare-ups" in western Qinling orogeny, China: New insights into the convergence history of the North and South China Blocks at the northern margin of Gondwana

Long Ren, Huaying Liang *, Zhiwei Bao *, Wenting Huang

Key Laboratory of Mineralogy and Metallogeny, Guangzhou Institute of Geochemistry, Chinese Academy of Sciences, Guangzhou 510640, China

ARTICLE INFO

Article history:
Received 28 March 2020
Received in revised form 7 September 2020
Accepted 9 October 2020
Available online 15 October 2020

Keywords:
Pulsed magmatism
Petrogenesis
Geodynamic evolution
Qinling Orogen
Gondwana

ABSTRACT

The geodynamic evolution of an accretionary orogeny commonly includes multiple magmatic episodes, which can be used to trace orogenic geodynamic processes using the geochronological and petrogenetic records preserved by igneous rocks. Paleomagnetic data indicate that the juxtaposed North China Craton (NCC) and South China Block (SCB) were located on the northern margin of the Gondwana supercontinent, but the geodynamic history of the two related blocks is still unclear. To address this issue, this paper integrates literature data with new geochronological, elemental, and isotopic data from early Paleozoic intermediate and silicic intrusions of the western North Qinling Terrane. We recognize three early Paleozoic flare-ups of intermediate–silicic intrusive magmatism in this area for the first time. Despite their similar lithology, the early Paleozoic igneous rocks formed during the three pulses have distinct geochemical compositions and petrogenesis, and record the evolution from subduction to continental collision. Geochronological data record: (1) An early Silurian (c. 441–434 Ma) pulse of diorite–quartz diorite–granite magmatism. The diorites and quartz diorites probably formed by fractionation of partial melts of mantle wedge modified by slab-derived hydrous fluids, while the granites formed by the partial melting of juvenile mafic lower crust. (2) A middle Silurian high-flux pulse of diorites, quartz diorites, and leucogranites (two-mica and muscovite granites) at c. 430–423 Ma. The diorites and quartz diorites were generated by crustal assimilation and fractional crystallization of basaltic partial melts of a pre-existing mantle source that had been altered by slab-derived hydrous fluids, and that was subsequently modified by slab-melts. The two-mica and muscovite granites formed by water-present melting of early–middle Silurian metamorphosed igneous rocks derived from enriched mantle and (meta-)graywackes, respectively. (3) A late Silurian (c. 415–409 Ma) magmatic pulse formed quartz diorites, A-type granites, and leucogranites (muscovite granites). The quartz diorites formed by differentiation of basaltic partial melts of enriched mantle, with a large contribution from depleted asthenospheric mantle. The A-type granites were generated by anatexis of juvenile mafic lower crust and subsequent fractional crystallization. The muscovite granites formed by biotite dehydration melting of (meta-)graywackes. The origins of these three early Paleozoic magmatic pulses were integrated with published regional paleomagnetic data and descriptions of sedimentary, metamorphic and igneous rocks, to provide a unique record of the geotectonic evolution of the Qinling Orogenic Belt that included: (1) slab roll-back at c. 448–434 Ma; (2) initial continental collision at c. 433 Ma; (3) slab break-off at c. 430–423 Ma; (4) small-scale lithospheric foundering in a post-collisional setting at c. 415–409 Ma. Literature-derived geochronological records of collision-related magmatism and paleomagnetic data indicate that docking of the NCC and SCB with the northern Gondwana margin probably ended during the early Silurian (c. 433 Ma).

1. Introduction

The Qinling Orogenic Belt is an important composite accretionary orogeny that lies between the North China Craton (NCC) and South China Block (SCB) in Asia. It records early Paleozoic and Mesozoic subduction and continental collision between the NCC and SCB (Dong et al., 2013). Given that the NCC and SCB converged on the northern margin of Gondwana (Dong et al., 2011), the early Paleozoic tectonic evolution of the Qinling Orogenic Belt is a critical element of Gondwana's configuration. However, the details of the collision are debated. For example, Liu et al. (2016) infer that closure of the Proto-Tethys Ocean (Shangdan Ocean), slab break-off, and post-collisional extension occurred around 500, 450, and 420 Ma, respectively, based on details of the high–ultrahigh pressure metamorphism of the eastern North Qinling Terrane (NQT). Dong et al. (2011, 2013) argued for Early Devonian

* Corresponding authors.
E-mail addresses: lianghy@gig.ac.cn (H. Liang), baozw@gig.ac.cn (Z. Bao).

https://doi.org/10.1016/j.lithos.2020.105833
0024-4937/

(c. 400 Ma) closure of the Proto-Tethys Ocean based on a Paleozoic ophiolite and associated rocks, and detrital zircons from clastic rocks in the NQT. In contrast, some scholars suggest that the spatio–temporal distribution of early Paleozoic intrusions records initial continental collision during the Late Ordovician (c. 450–440 Ma) (Wang et al., 2013), and others have concluded that the NCC and SCB did not collide in the early Paleozoic (Huang et al., 2018; Wu and Zheng, 2013).

There is consensus that evolving arcs are characterized by the "steady state" magmatism associated with weak mantle thermal fluxes, low magmatic addition rates and normal geothermal gradients, which is often punctuated by ephemeral and high-capacity magmatism (de Silva et al., 2015). Therefore, the concept of flare-ups was developed to explain increased rates of magma production, which are commonly initiated by changes in the geometry and geodynamics of subduction zones and lithospheric processes, such as slab rollback, slab break-off, slab tearing, crustal thickening, and lithospheric delamination (DeCelles et al., 2009). In this paper, the concept is extended to include high-flux pulses of magmatism corresponding to major geodynamic changes in accretionary orogenic processes. If flare-ups are responses to orogenic processes and tectonic evolution, then the genesis of early Paleozoic magmatic flare-ups within the western NQT might record details of the geodynamic evolution and convergence of the NCC and SCB on the northern Gondwana margin.

We performed a detailed petrographic, geochronological, geochemical, and isotopic investigation of six early Paleozoic intermediate–silicic intrusions, and compiled published geochemical data from other intrusions in the western NQT (Pei et al., 2007a; Ren et al., 2018; Wang, 2013; Wang et al., 2008; Wei et al., 2012; Wu et al., 2018; Xu et al., 2017; Yang, 2017; Zhang et al., 2006). The objectives were to: (1) elucidate the episodic nature of early Paleozoic intermediate–silicic intrusive magmatism; (2) delineate the early Paleozoic geodynamic evolution of the Qinling Orogenic Belt; and (3) reconstruct the convergence of the NCC and SCB with the northern margin of Gondwana.

2. Geological background

The Qinling Orogenic Belt of central China has a complex history that involved multiple stages of subduction, continental collision, and continent–arc collision from the Neoproterozoic to Mesozoic (Dong et al., 2016). Continental collision between the NCC and SCB formed the early Paleozoic Shangdan and Triassic Mianlue sutures in this belt; these separate the NQT, South Qinling Terrane, and SCB (Fig. 1; Wu and Zheng, 2013).

The western segment of the Qinling Orogen, located west of 108° longitude (Zhang et al., 2002), is commonly referred to as the Western Qinling Orogenic Belt. The crystalline basement of the NQT in this belt includes the late Mesoproterozoic to early Neoproterozoic Qinling and Longshan groups; both of these include gneisses, amphibolites, and marble, and underwent early Paleozoic greenschist–amphibolite facies metamorphism (Fig. 2; Liu, 2013; Yu et al., 2016). In addition, voluminous Neoproterozoic and early Paleozoic meta-volcanic–sedimentary rocks crop out in the NQT. These include the Kuanping, Erlangping, and Danfeng groups (Dong et al., 2011; Wu and Zheng, 2013). The Danfeng Group, also known as the Shangdan suture zone, consists mainly of ophiolite mélange and arc-related igneous rocks (Li et al., 2015). It is exposed discontinuously on the southern margin of the NQT and was metamorphosed under greenschist–amphibolite conditions (Dong et al., 2011; Wu and Zheng, 2013).

3. Petrographic description and samples

The early Paleozoic intermediate–silicic intrusions of the western NQT are mainly diorites, quartz diorites, and metaluminous and peraluminous granites. Six representative intermediate–silicic intrusions, which include all of these rock types, were investigated for this study (Fig. 2).

The Huangniupu pluton crops out over an area of ~200 km^2, intrudes Ordovician strata, and consists of coarse-grained quartz diorite that

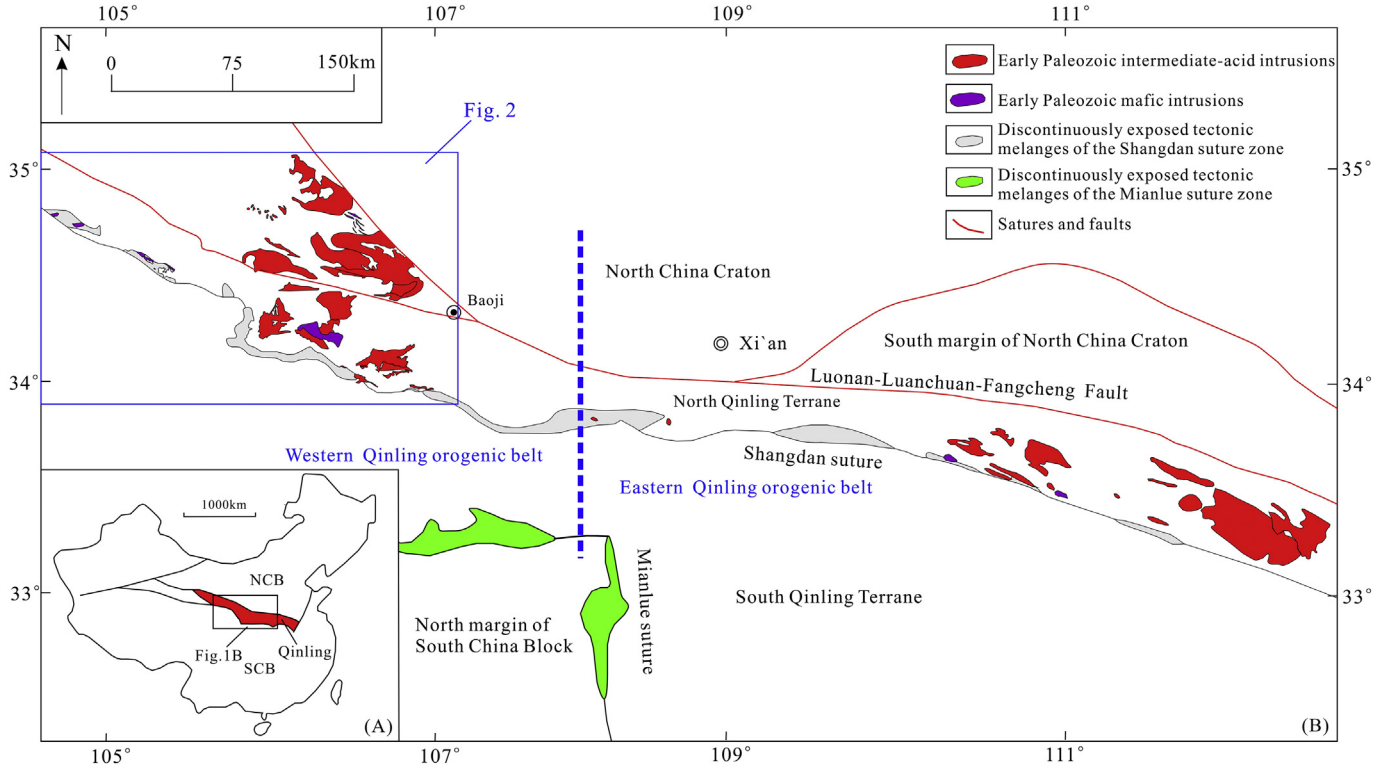

Fig. 1. The location (A) and tectonic framework (B) of the Qinling orogenic belt, central China. Modified from Wang et al., 2013.

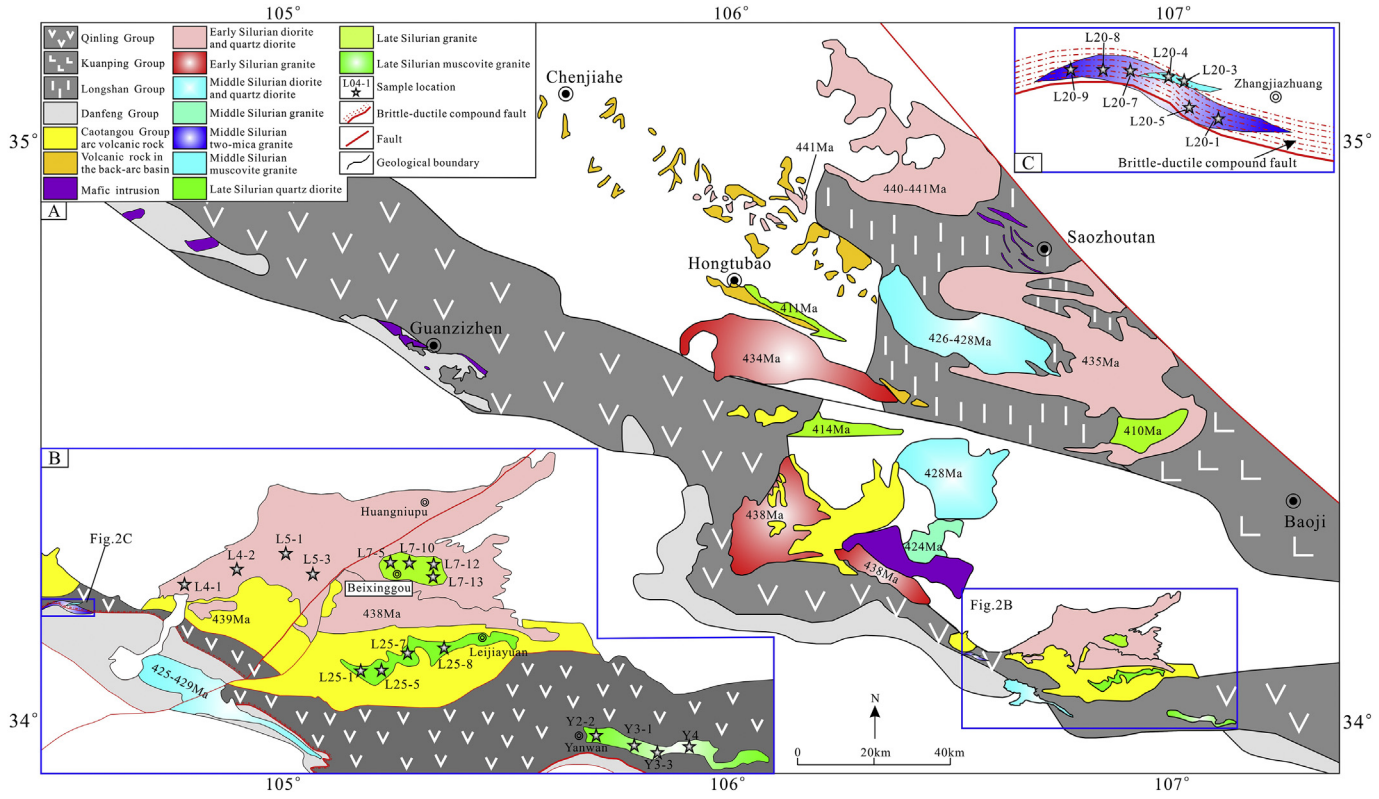

Fig. 2. Simplified geological map of the western part of Qinling orogen.
Revised from Liu, 2013.

comprises plagioclase (~60%), K-feldspar (~7%), quartz (~13%), hornblende (~15%), and biotite (~5%), with accessory magnetite, titanite, apatite, allanite, and zircon (Fig. 3A). Mafic microgranular enclaves (MMEs) are widely distributed and comprise plagioclase (~53%), hornblende (~40%), quartz (~5%), and acicular apatite (~2%), and have poikilitic igneous textures (Fig. 3B, C).

The Zhangjiazhuang granite pluton crops out over an area of ~3 km^2 and consists of two-mica granite and muscovite granite. The two-mica granite intrudes Qinling Group gneiss and the Danfeng Group (Figs. 2B, 3D), and is intruded by the muscovite granite (Fig. 3F). The rocks are medium–fine grained and strongly foliated. The two-mica granite consists of plagioclase (~34%), quartz (~34%), K-feldspar (~21%), muscovite (~7%), and biotite (~4%) (Fig. 3E). The muscovite granite consists of plagioclase (~26%), K-feldspar (~24%), quartz (~35%), and muscovite (~15%) (Fig. 3G). Both granites contain accessory magnetite, titanite, and zircon.

The Leijiayuan pluton crops out over an area of ~30 km^2, intrudes Ordovician strata, and consists of a medium-grained quartz diorite (Fig. 3H) that comprises quartz (~15%), plagioclase (~55%), K-feldspar (~7%), and hornblende (~23%), with accessory magnetite, titanite, apatite, allanite, and zircon. The hornblende is extensively chloritized (Fig. 3I).

The Beixinggou granite crops out over an area of ~15 km^2 and intrudes the Huangniupu quartz diorite. It is medium–coarse grained and consists of quartz (~45%), K-feldspar (~39%), plagioclase (~10%), and biotite (~6%), with accessory apatite, titanite, zircon and magnetite (Fig. 3J).

The Yanwan muscovite granite crops out over an area of ~30 km^2 and intrudes the Qinling Group gneisses (Fig. 3K). It is medium- to fine-grained and comprises plagioclase (~26%), K-feldspar (~29%), quartz (~34%), and muscovite (~11%), with accessory magnetite, titanite, and zircon (Fig. 3L).

4. Analytical methods

Zircon grains from ~1.5 kg of each of six samples were separated by conventional heavy-liquid separation and magnetic–gravimetric techniques and mounted in epoxy at the Guangzhou Institute of Geochemistry, Chinese Academy of Sciences (GIGCAS). The U-Pb zircon data were analyzed by laser ablation-inductively coupled plasma-mass spectroscopy (LA-ICP-MS) at the GIGCAS. Zircon 91,500 and the NIST 610 reference material were used as standards for age calibration and elemental analyses, respectively. Zircon U–Th–Pb data were processed with the ISOPLOT software to produce concordia plots. The U-Pb age of the main zircon populations are interpreted as the timing of intrusion crystallization.

In-situ zircon Hf isotopic data were analyzed by a Neptune Plus multi-collector ICP–MS (MC-ICP-MS) and RESOlution M-50 laser ablation system at the GIGCAS. Spot selection for Lu-Hf analysis was based on the zircon U-Pb ages and cathodoluminescence (CL) images, which differentiated igneous from xenocrystic zircons. Additionally, large igneous and xenocrystic zircons were selected for Hf isotopic analysis. The Penglai zircon was used as a reference standard and yielded a weighted mean $^{176}Hf/^{177}Hf$ ratio of 0.282901 ± 0.000011 (2SD; $n = 16$), which is within experimental error of the recommended value of Li et al. (2010a).

Fresh samples were powdered to ~200 mesh in an agate mortar. Major elements were analyzed by X-ray fluorescence (XRF) on a Rigaku RIX 2000 instrument, and the trace elements were analyzed by a Bruker M90 ICP–MS instrument at the GIGCAS. Analytical uncertainties on the major and trace elements are approximately ±1%–2% and better than ± 5%–10%, respectively.

Strontium and rare earth elements (REEs) were separated by conventional ion exchange columns and Nd was separated by HDEHP-coated Kef columns. The Sr and Nd isotope ratios were

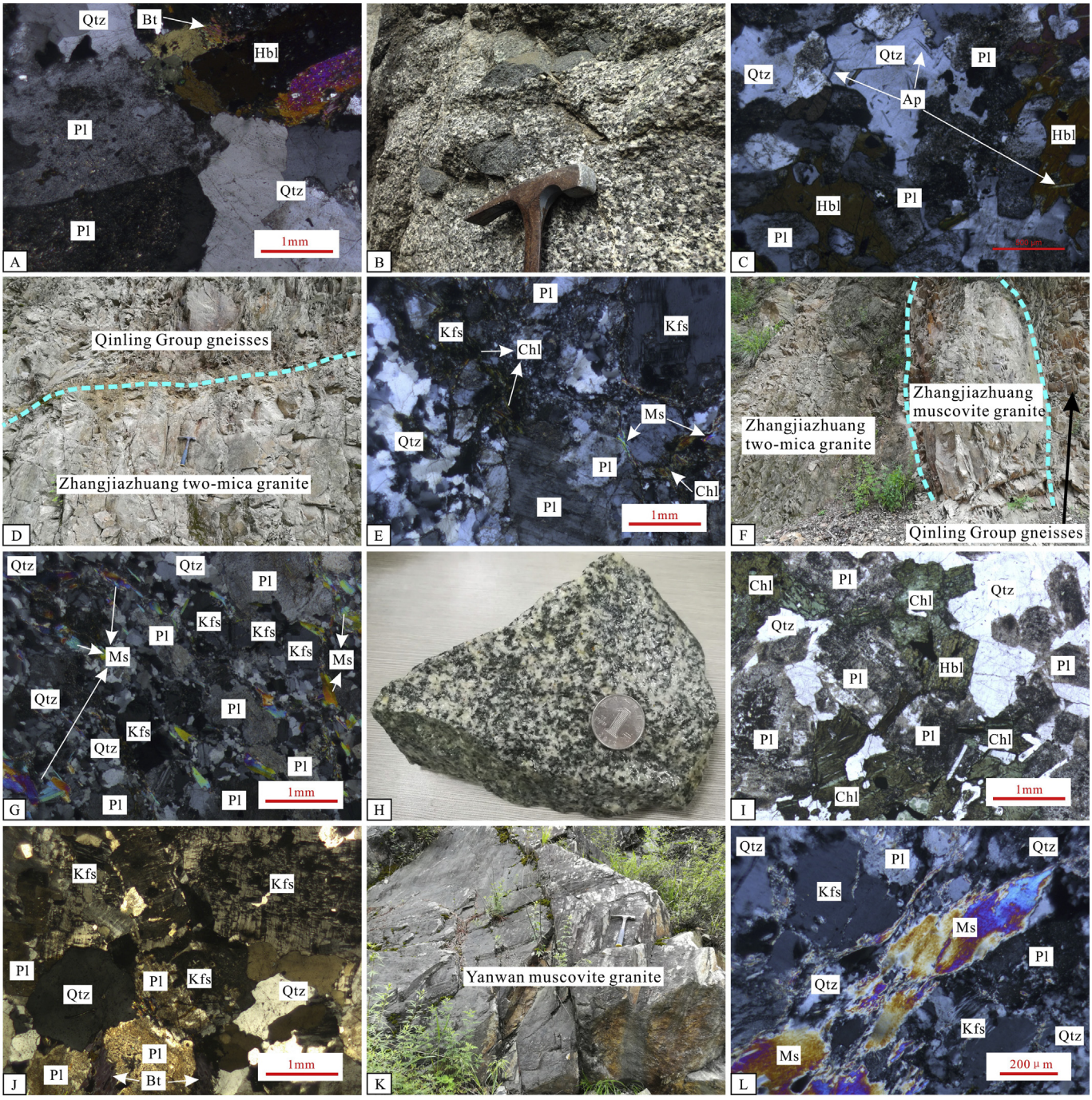

Fig. 3. Representative field occurrence and thin section petrography of the studied intrusions: (A) microphotograph of the Huangniupu intrusion; (B–C) the field occurrence and microphotograph of MMEs in the Huangniupu quartz diorite; (D) the Zhangjiazhuang two-mica granite intrudes the Qinling group gneisses; (E) photomicrograph of the Zhangjiazhuang two-mica granite; (F) the Zhangjiazhuang muscovite granite intrudes the two-mica granite and Qinling group gneisses; (G) microphotograph of the Zhangjiazhuang muscovite granite; (H–I) specimen and microphotograph of the Leijiayuan quartz diorite; (J) microphotograph of the Beixinggou biotite granite; (K) field photograph of Yanwan muscovite granite; (L) microphotograph of the Yanwan muscovite granite. Abbreviations: Qtz = Quartz; Pl = Plagioclase; Kfs = K-feldspar; Hbl = Hornblende; Bt = Biotite; Ms. = Muscovite; Ap = apatite; Chl = chlorite.

analyzed by MC–ICP–MS. The BHVO-2 and JG-2 standards yielded $^{87}Sr/^{86}Sr = 0.703472 \pm 0.000023$ (2σ, $n = 13$) and $^{143}Nd/^{144}Nd = 0.512217 \pm 0.000011$ (2σ, n = 13), respectively.

5. Results

5.1. U-Pb ages

All zircons from the six intrusions are euhedral and prismatic (Fig. 4), have high Th/U ratios of 0.07–3.10 (Supplementary Table 1), and show typical oscillatory zoning (Fig. 4), indicating an igneous origin. Eighteen LA-ICP-MS U-Pb ages of zircon from the Huangniupu quartz diorite yield a $^{206}Pb/^{238}U$ age of 440 ± 3 Ma (MSWD = 0.10; Fig. 4A). Thirty zircons from the Zhangjiazhuang two-mica granite were analyzed. Nine discordant results and four older grains (776–476 Ma) assumed to represent inherited or xenocrystic zircons were excluded. The remaining 17 analyses yield a $^{206}Pb/^{238}U$ age of 430 ± 2 Ma (MSWD = 0.40; Fig. 4B). Thirty zircon crystals from the Zhangjiazhuang muscovite granite were analyzed. Three discordant results and twelve older zircons (2254–725 Ma) assumed to represent inherited or

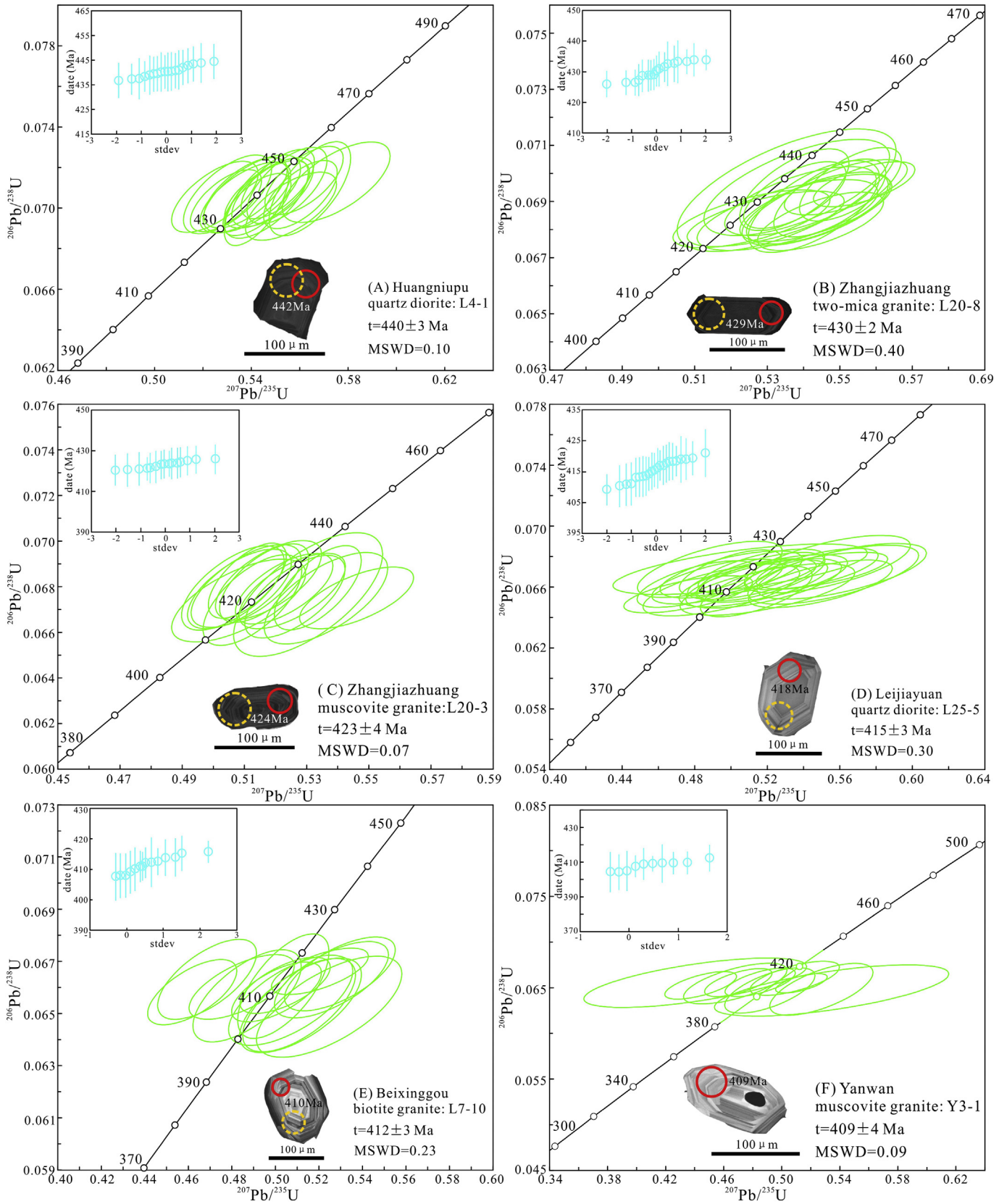

Fig. 4. Zircon U-Pb concordia plots for the studied intrusions, with the red solid and yellow dotted circles representing in-situ U-Pb age and Lu-Hf isotope analyses, respectively. Insets show cumulative probability plots and representative cathodoluminescence images.

xenocrystic zircons were excluded from further analysis. The remaining fifteen analyses yield a $^{206}Pb/^{238}U$ age of 423 ± 4 Ma (MSWD = 0.07; Fig. 4C). Twenty-three zircons from the Leijiayuan quartz diorite were analyzed, and an older grain (435 ± 8 Ma) assumed to represent inherited or xenocrystic zircon was excluded. The remaining 22 analyses yield a $^{206}Pb/^{238}U$ age of 415 ± 3 Ma (MSWD = 0.30; Fig. 4D). Sixteen analyses of zircon from the Beixinggou biotite granite were performed. One discordant analysis and one younger age (352 ± 6 Ma) assumed to record Pb-loss were excluded. The remaining 14 crystals yield a $^{206}Pb/^{238}U$ age of 412 ± 3 Ma (MSWD = 0.23; Fig. 4E). Twenty-five analyses of zircon from the Yanwan muscovite granite produced eight discordant analyses, four older ages (865–454 Ma) assumed to represent inherited or xenocrystic zircons, and three relatively young ages (357–307 Ma) assumed to record Pb-loss were excluded from further analysis. The remaining ten analyses yield a $^{206}Pb/^{238}U$ age of 409 ± 4 Ma (MSWD = 0.09; Fig. 4F).

Integration of our new data with published geochronological information reveal that there were three pulses of intermediate–silicic intrusive magmatism in the western NQT at 441–434 Ma (early Silurian), 430–423 Ma (middle Silurian), and 415–409 Ma (late Silurian) (Fig. 5).

5.2. Whole-rock geochemistry

Our new major and trace element compositions are shown in Supplementary Table 2. The Leijiayuan quartz diorites have high loss on ignition values (2.12–5.90 wt%) that are attributed to chloritization without element mobilization, and therefore, their analyses are normalized to the totals of anhydrous oxides.

5.2.1. Early Silurian intrusions

The early Silurian intrusive rocks are mainly diorites, quartz diorites, and granites that define a bimodal distribution (Fig. 6A). They have relatively high K_2O contents (2.09–5.33 wt%), low FeOt/(FeOt + MgO) values (0.51–0.80), plot in the fields of high-K calc-alkaline rocks and shoshonites, and are classified as magnesian rocks (Fig. 6B, D). The diorites and quartz diorites are metaluminous and have lower A/CNK (Al_2O_3/CaO + Na_2O + K_2O) values (0.73–0.95) than the weakly peraluminous granites (1.03–1.15) (Fig. 6C). The diorite, quartz diorite, and granite trace element data plot as sub-parallel lines on plots of incompatible and rare earth elements, and are characterized by enriched light REEs and large-ion-lithophile elements (LILEs), depleted heavy REEs (HREEs) and high-field-strength elements (HFSEs), and weak Eu anomalies (Fig. 7 A, B).

5.2.2. Middle Silurian intrusions

The middle Silurian rocks are mostly diorites, quartz diorites, and two-mica and muscovite peraluminous granites. The diorite and quartz diorites have relatively low A/CNK (0.72–1.02) and FeOt/(FeOt + MgO) values (0.55–0.66), are classified as metaluminous and magnesian (Fig. 6C, D), enriched in LREEs and LILEs, depleted in HREEs and HFSEs, and show negligible Eu anomalies (Eu/Eu* = 0.77–1.04). They have lower K_2O contents (1.17–3.50 wt%) than the early Silurian diorite and quartz diorites (2.09–5.33 wt%) and are classified as calc-alkaline to high-K calc-alkaline (Fig. 6B). The REE patterns are more fractionated ($(La/Yb)_N$ = 34.7–166) than the early Silurian diorites and quartz diorites ($(La/Yb)_N$ = 7.26–17.4) (Fig. 7A, C).

Overall, the middle Silurian two-mica and muscovite granites have high A/CNK values of 1.10–1.31, FeOt/(FeOt + MgO) ratios of 0.80–0.88, and are classified as peraluminous ferroan granites (Fig. 6C, D). They are enriched in LILEs and depleted in HFSEs (Fig. 7D). The two-mica granites have higher Al_2O_3 (15.02–15.66 wt%) and Na_2O (4.01–4.88 wt%), and lower K_2O contents (3.33–3.74 wt%) than the muscovite granites (13.90–14.04 wt%, 2.78–2.79 wt%, and 4.80–4.87 wt%, respectively) (Fig. 6B). Furthermore, the two-mica granites have high La (31.5–41.3 ppm) and low Yb contents (0.46–0.57 ppm), fractionated REE patterns ($(La/Yb)_N$ = 42.6–52.9), and negligible Eu anomalies (Eu/Eu* = 0.70–0.97). In contrast, the muscovite granites have low La (19.3–20.2 ppm) and high Yb contents (0.74–0.75 ppm), less-fractionated REE patterns ($(La/Yb)_N$ = 18.7–19.3), and moderately negative Eu anomalies (Eu/Eu* = 0.47–0.52) (Fig. 7C).

5.2.3. Late Silurian intrusions

The late Silurian rocks consist predominantly of granites, with minor quartz diorites. The quartz diorites have relatively low FeOt/(FeOt + MgO) (0.66–0.67) and A/CNK values (0.86–0.94), are classified as metaluminous and magnesian (Fig. 6C, D), and are enriched in LREEs, depleted in HREEs, and show small negative Eu anomalies (Eu/Eu* = 0.57–0.66) (Fig. 7E).

The late Silurian granites are metaluminous to weakly peraluminous granites (A/CNK = 0.98–1.05; Fig. 6C) and peraluminous muscovite granites (A/CNK = 1.07–1.31; Fig. 6C). Most of them plot within the fields of the high-K calc-alkaline to shoshonitic series (Fig. 6B) and have high FeOt/(FeOt + MgO) ratios (0.79–0.88) that plot on the boundary between the ferroan and magnesian fields (Fig. 6D). They are enriched in LREEs, depleted in HFSEs, and have strong negative Eu anomalies (Eu/Eu* = 0.21–0.77) (Fig. 7E, F).

5.3. Radiogenic isotope data

Our new whole-rock Sr-Nd and zircon in-situ Hf radiogenic data from early Paleozoic intermediate–silicic intrusions are provided in Supplementary Tables 3 and 4, respectively.

5.3.1. Early Silurian intrusions

The diorites and quartz diorites have initial Sr isotope ratios of 0.70457–0.70635, $\varepsilon_{Nd}(t)$ values of −0.65 to −3.60, and $\varepsilon_{Hf}(t)$ values of 1.90 to 6.06, which are similar to those of the granites ($(^{87}Sr/^{86}Sr)_i$ = 0.70396 to 0.70929; $\varepsilon_{Nd}(t)$ = −0.30 to −4.48; $\varepsilon_{Hf}(t)$ = −1.18 to 5.77 (Fig. 8A, B).

5.3.2. Middle Silurian intrusions

The diorites and quartz diorites have initial Sr isotope ratios of 0.70316–0.70619, $\varepsilon_{Nd}(t)$ values of −0.74 to −3.18, and $\varepsilon_{Hf}(t)$ values of 1.03 to 6.20, which are similar to those of the early Silurian diorites and quartz diorites (Fig. 8A, B). The two-mica granites have lower $(^{87}Sr/^{86}Sr)_i$ values (0.70715 to 0.70804) but higher $\varepsilon_{Nd}(t)$ and $\varepsilon_{Hf}(t)$ values (−2.02 to −3.14 and − 1.15 to 6.48, respectively) than the muscovite granites ($(^{87}Sr/^{86}Sr)_i$ = 0.71285 to 0.71334, $\varepsilon_{Nd}(t)$ = −3.49 to −3.63, $\varepsilon_{Hf}(t)$ = −6.61 to −0.44)(Fig. 8A, B). The xenocrystic zircons (1124–825 Ma) from the muscovite granites have significantly lower $\varepsilon_{Hf}(t)$ values of −21.6 to −14.2 (Fig. 8B).

5.3.3. Late Silurian intrusions

The late Silurian quartz diorites have more depleted isotopic compositions than the early–middle Silurian diorites and quartz diorites, with $(^{87}Sr/^{86}Sr)_i$ ratios of 0.70473 to 0.70505, $\varepsilon_{Nd}(t)$ values of 1.39 to 1.83, and $\varepsilon_{Hf}(t)$ values of 7.73 to 11.2 (Fig. 8A, B). The granites have extremely low $(^{87}Sr/^{86}Sr)_i$ ratios of 0.69615 to 0.70119, which are attributed to high Rb/Sr values (3.93–2.01) and are not discussed further. The isotopic composition of the granites is also depleted relative to the early Silurian granites ($\varepsilon_{Nd}(t)$ = −2.61 to −1.97; $\varepsilon_{Hf}(t)$ = 3.55 to 8.91), compared with $\varepsilon_{Nd}(t)$ values of −4.48 to −0.30 and $\varepsilon_{Hf}(t)$ values of −1.18 to 5.77 for the earlier granites. In addition, the muscovite granites show a similar degree of isotopic evolution ($(^{87}Sr/^{86}Sr)_i$ = 0.71044 to 0.71126, $\varepsilon_{Nd}(t)$ = −5.35 to −4.15) to the middle Silurian muscovite granites (Fig. 8A).

6. Discussion

6.1. Episodic magmatism in the North Qinling Terrane

There are three pulses of early Paleozoic intermediate–silicic intrusive activity in the western part of the NQT. The duration of the early Silurian pulse was eight million years, from c. 441 Ma to c. 434 Ma, and

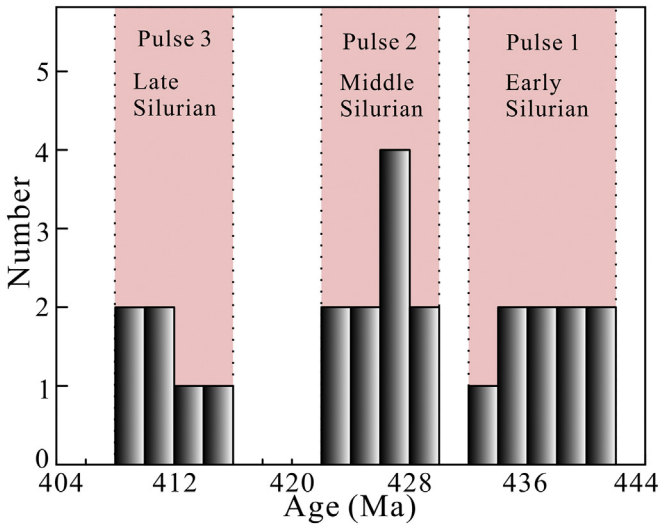

Fig. 5. Three phases of early Paleozoic intermediate–silicic magmatism in the western NQT.

involved the formation of granites (438–434 Ma), diorites, and quartz diorites (441–435 Ma; Fig. 2). The middle Silurian pulse also lasted for eight million years, from c. 430 Ma to c. 423 Ma, and is represented by extensive diorites and quartz diorites, with minor two-mica and muscovite granites (Fig. 2). The late Silurian pulse lasted for seven million years, from c. 415 Ma to c. 409 Ma, and is represented by quartz diorites (415 Ma), granites (414–410 Ma), and muscovite granites (409 Ma).

6.2. Petrogenesis of the early Silurian intrusions

The diorites and quartz diorites might have formed by melting of an oceanic slab or continental crust, or fractionation of basaltic magma (Annen et al., 2006; Martin et al., 2005). Slab melts commonly have high Sr/Y and $(La/Yb)_N$ ratios ($Y \leq 18$ ppm; $Yb \leq 1.8$ ppm) and Na_2O contents ($3.5 \leq Na_2O \leq 7.5$ wt%), low K_2O/Na_2O ratios (~0.42) (Martin et al., 2005; Moyen and Martin, 2012), which are inconsistent with the high Y (16.3–28.1 ppm) and Yb (1.59–2.53 ppm) contents and K_2O/Na_2O (0.49–1.31) ratios of the early Silurian diorites and quartz diorites. Additionally, the lower crust and crystalline basement of the NQT, which are formed by the Qinling Group, have significantly lower Sr–Nd–Hf isotopic ratios than the diorites and quartz diorites (Fig. 8A, B). Therefore, the early Silurian diorites and quartz diorites are not partial melts of the continental or oceanic crust. The diorites and quartz diorites have

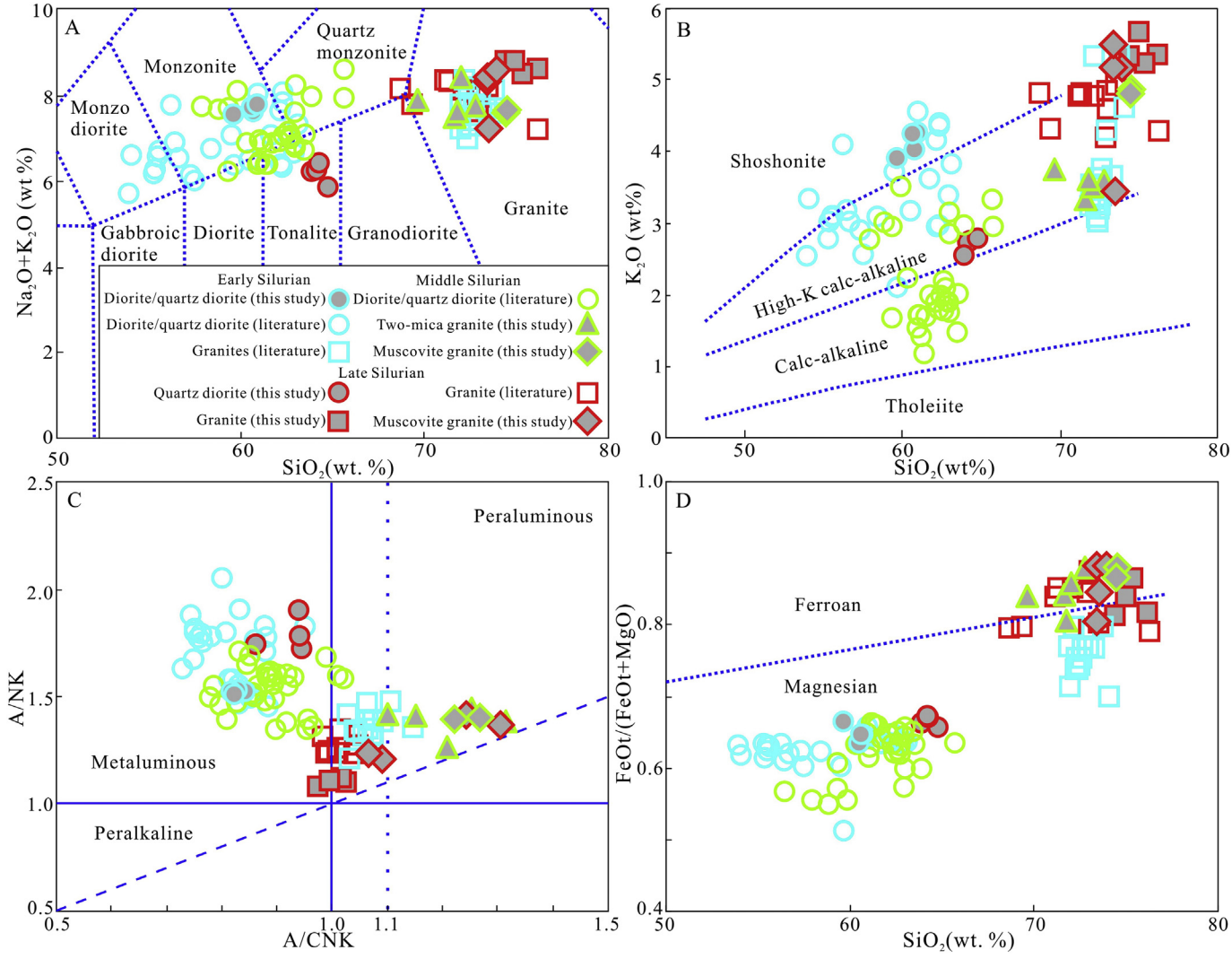

Fig. 6. (A) Total alkali–silica (TAS) diagram; (B) Plot of K_2O vs. SiO_2; (C) $Al_2O_3/(Na_2O + K_2O)$ molar vs. $Al_2O_3/(CaO + Na_2O + K_2O)$ molar plot; (D) Ferroan–magnesian granitoid classification (Frost et al., 2001).

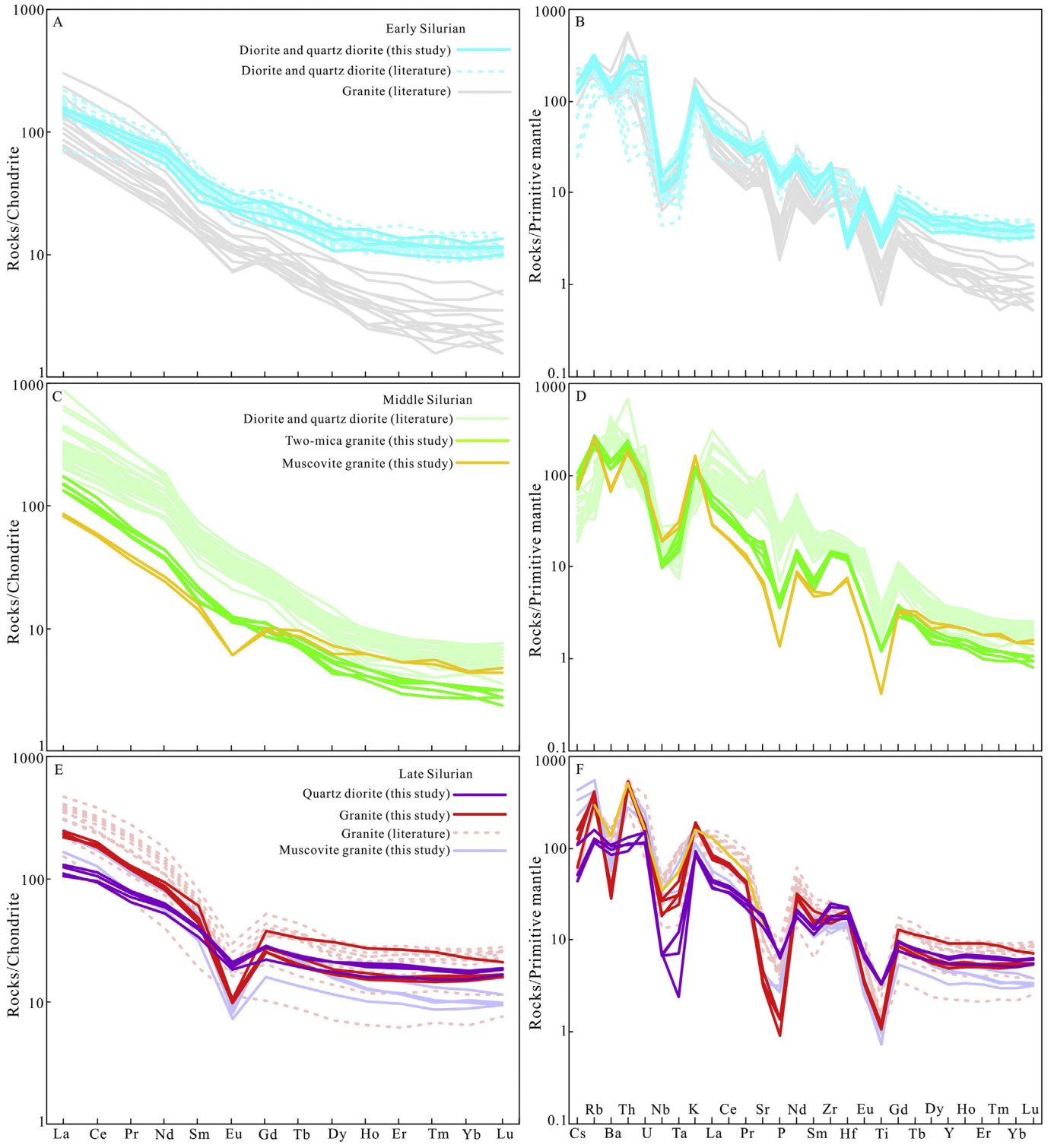

Fig. 7. Incompatible and rare earth element compositions normalized to (A, C, E) chondrite and (B, D, F) primitive mantle.

high Ba and Sr contents (671–1272 ppm and 555–969 ppm, respectively) and low Rb contents (59.0–213 ppm), fractionated REE profiles (Fig. 7A), small Eu anomalies and strong negative Nb and Ta anomalies (Fig. 7B), consistent with the characteristics of high Ba-Sr granitoids (Fig. 9A). These rocks are thought to originate from an enriched mantle (Fowler et al., 2008). Therefore, we infer that the early Silurian diorites and quartz diorites derive from enriched mantle, based on: (1) Sr-Nd isotopic compositions that plot between contemporaneous back-arc basin basalts and enriched-mantle-derived mafic rocks (Fig. 8A); and (2) the high Ba (537–3322 ppm) and Sr (315–1418 ppm) contents of Ordovician mafic intrusions derived from enriched mantle in the NQT (Li, 2008; Wang et al., 2014). Slab-derived fluids transport mainly water-soluble elements, while hydrous melts transfer water-soluble and water-insoluble elements (Ren et al., 2019; Zheng, 2012). Plots of Rb/Zr vs. Nb/Zr and Rb/Y vs. Nb/Y show that the diorites and quartz diorites were derived from enriched mantle modified by slab-derived hydrous fluids (Fig. 9B, C). Additionally, increasing SiO_2 is related to constant Na_2O and Al_2O_3 concentrations, high K_2O, Zr, Ce, and Nb

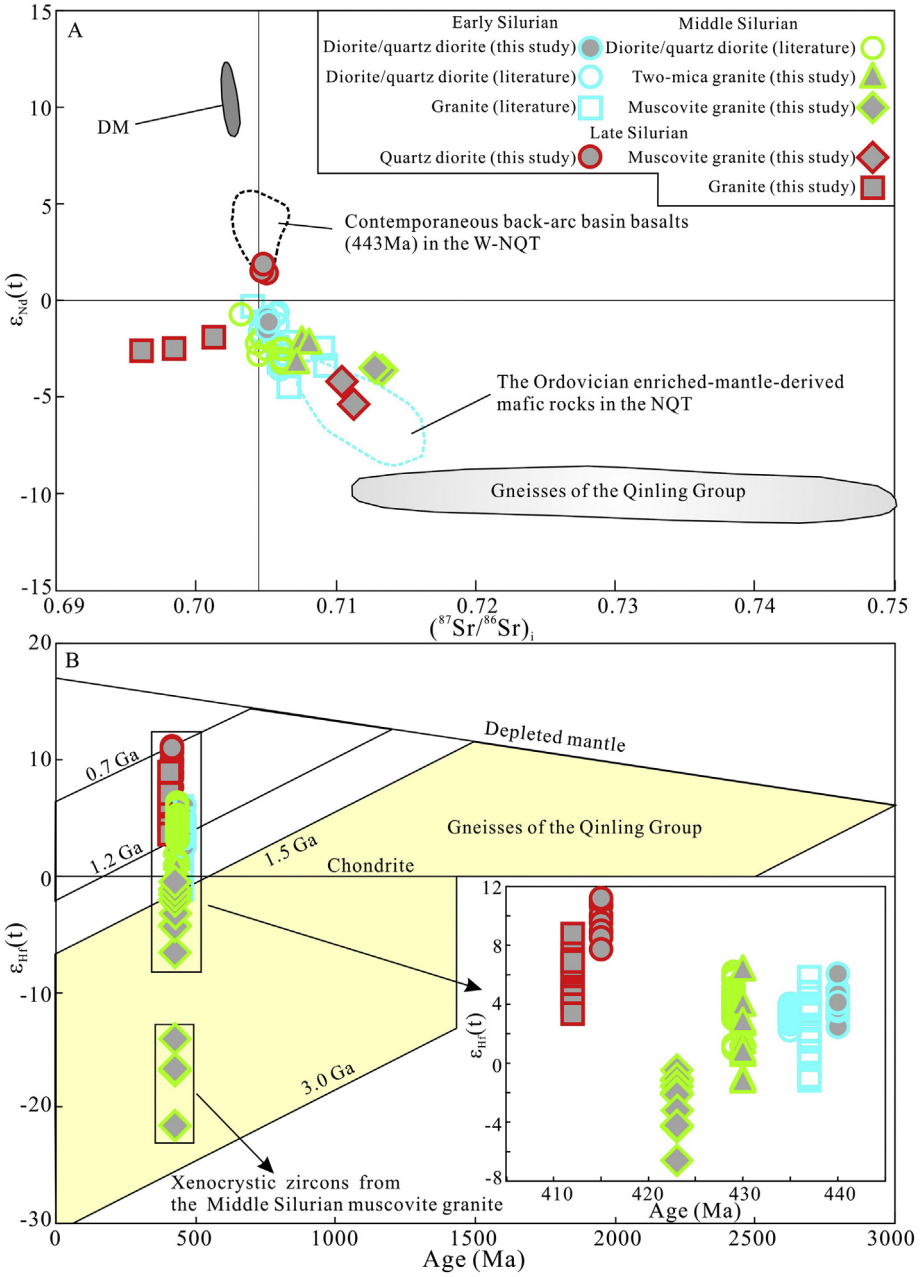

Fig. 8. (A) Sr-Nd isotopes for the early Paleozoic intermediate–silicic intrusions, DM (depleted mantle), Qinling Group gneisses, and the Ordovician enriched mantle in the NQT. Sr and Nd isotopic compositions are calculated at $t = 420$ Ma. (B) Diagram of zircon Hf isotopes vs. ages.

contents, and low MgO, CaO, and P_2O_5 concentrations (Fig. 9E–L), consistent with fractionation of mafic minerals and apatite. The $\varepsilon_{Nd}(t)$ values are independent of the SiO_2 content (Fig. 9D), which indicates that crustal assimilation was negligible.

Large volumes of granite are generally thought to form by partial melting of crustal material (Clemens and Stevens, 2012). The early Silurian granites have Sr–Nd–Hf isotopic compositions similar to the contemporaneous diorites and quartz diorites, but different from the crystalline basement of the NQT (Fig. 8A, B), which indicates that the most likely source is juvenile mafic lower crust. This inference is consistent with the similar incompatible and rare earth element plots for the diorites, quartz diorites, and granites (Fig. 7A, B).

In summary, we infer that the early Silurian diorites and quartz diorites are likely to have formed by fractionation of partial melts of mantle modified by slab-derived hydrous fluids, and that the granites formed by partial melting of juvenile mafic lower crust.

6.3. Petrogenesis of the middle Silurian intrusions

6.3.1. Diorites and quartz diorites

The middle Silurian diorites and quartz diorites have high Ba (1384–3050 ppm) and Sr (655–2376 ppm) contents, low Rb contents (21.0–144 ppm), fractionated REE patterns, small Eu anomalies, and enriched isotopic compositions ($(^{87}Sr/^{86}Sr)_i$ = 0.70316–0.70619, $\varepsilon_{Nd}(t) = -3.18$ to -0.74, $\varepsilon_{Hf}(t) = 1.03$–6.20), similar to those of the early Silurian diorites and quartz diorites (Figs. 7C, D, 8A, B, 9A), which indicate that they are likely to have formed from mantle that has interacted with slab-derived hydrous fluids. However, some geochemical features are unique to the middle Silurian rocks. These include: (1) lower K_2O contents and higher Na_2O, Na_2O/K_2O, and P_2O_5 values than the early Silurian diorites and quartz diorites (Figs. 6B, 9G–I); (2) more fractionated REE patterns and higher La/Yb values than the early Silurian diorites and quartz diorites (Figs. 7A, C, 9J); and

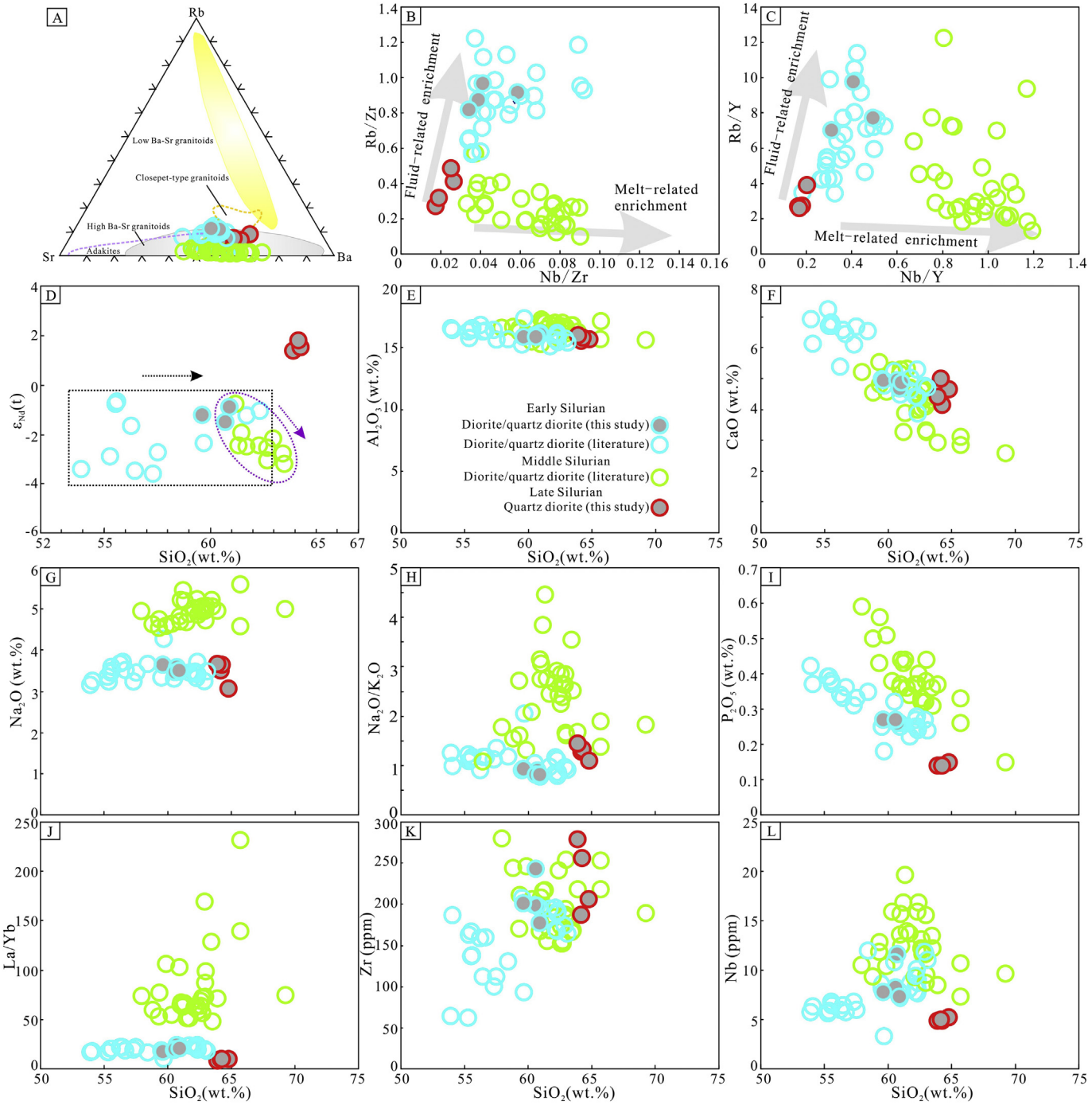

Fig. 9. Geochemical diagrams of the Silurian diorite/quartz diorites in the western NQT: (A) discrimination diagram of high Ba-Sr granitoids; (B–C) plots of Rb/Zr vs. Nb/Zr and Rb/Y vs. Nb/Y; (D) plots of Nd isotopes vs. SiO_2 contents; (E–L) harker diagrams.

(3) higher HFSEs (e.g., Zr, Nb) contents than the early Silurian diorites and quartz diorites (Fig. 9K, L). Slab-melt-derived adakites have high Na_2O ($3.5 \le Na_2O \le 7.5$ wt%), Na_2O/K_2O, and $(La/Yb)_N$ values of ~2.38 and > 10, respectively, and fractionated REEs. Niobium-enriched basalts derived from enriched mantle modified by slab-melts have high Nb, P_2O_5, and HFSE contents, and low LILE/HFSE and HREE/HFSE ratios (Martin et al., 2005; Sajona et al., 1994). The unique geochemical signatures of the middle Silurian intrusions indicate that slab-melts probably affected the mantle source of the middle Silurian diorites and quartz diorites. This inference is supported by plots of Nb/Y vs. Rb/Y and Nb/Zr vs. Rb/Zr, which indicate that the mantle source was modified by slab-derived fluids and melts (Fig. 9B, C). Given their younger emplacement ages than the early Silurian intrusions, we infer that the middle Silurian diorites and quartz diorites were derived from mantle that had been altered by slab-derived hydrous fluids, and that was subsequently modified by slab-melts. With increasing SiO_2 content, Na_2O and Al_2O_3 remain approximately constant, and CaO, MgO, Fe_2O_3 and P_2O_5 decrease (Fig. 9E–I), consistent with fractionation of mafic minerals and apatite. The value of $\varepsilon_{Nd}(t)$ decreases with increasing SiO_2 (Fig. 9D), consistent with crustal contamination.

6.3.2. Two-mica and muscovite granites

The middle Silurian two-mica and muscovite granites consist of quartz + plagioclase + K-feldspar + muscovite ± biotite, and are similar to leucogranites (Wu et al., 2015). They differ in the following details: (1) the two-mica granites have higher Al_2O_3 (15.02–15.66 wt%), Na_2O (4.01–4.88 wt%) and Na_2O/K_2O values (1.10–1.39) than the muscovite granites (13.90–14.04 wt%, 2.78–2.79 wt% and 0.57–0.58, respectively) (Fig. 10A, B); (2) the two-mica granites have higher Sr (210–401 ppm) and Ba (808–1010 ppm) contents and Sr/Y ratios (29.2–62.7), and lower Y contents (6.40–7.70 ppm) and Rb/Sr ratios (0.31–0.81) than the muscovite granites (Sr = 132–146 ppm; Ba = 464–488 ppm; Sr/Y = 12.3–14.0; Y = 10.4–10.7 ppm; Rb/Sr = 1.11–1.24; Fig. 10C–E); (3) the two-mica granites have higher La contents (31.5–41.3 ppm), lower Yb contents (0.46–0.57 ppm), and more fractionated REEs ($(La/Yb)_N$ = 42.6–52.9) than the muscovite granites (La = 19.3–20.2 ppm; Yb = 0.74–0.75 ppm; $(La/Yb)_N$ = 18.7–19.3), and the Eu anomalies are negligible (Eu/Eu* = 0.70–0.97) and slightly negative (Eu/Eu* = 0.47–0.52), respectively (Figs. 7C, 10E); and (4) the two-mica granites have lower $(^{87}Sr/^{86}Sr)_i$ values (0.70715 to 0.70804) but higher $\varepsilon_{Nd}(t)$ and $\varepsilon_{Hf}(t)$ values (−3.14 to −2.02 and − 1.15 to 6.48, respectively) than the muscovite granites ($(^{87}Sr/^{86}Sr)_i$ = 0.71285 to 0.71334, $\varepsilon_{Nd}(t)$ = −3.63 to −3.49, $\varepsilon_{Hf}(t)$ = −6.61 to −0.44) (Fig. 8A, B). These differences indicate that the two-mica and muscovite granites formed by different processes.

6.3.2.1. Two-mica granite. Adakitic characteristics, such as high Sr and La contents, low Y and Yb contents, and small Eu anomalies (Figs. 7C, 10E) indicate that the two-mica granites might be partial melts of thickened crust. However, melts of thickened lower crust have high $(Gd/Yb)_N$ ratios (>5.8; Huang and He, 2010) because Er, Tm, Yb, and Lu partition more strongly into garnet than other REEs (Moyen and Martin, 2012), which are distinct from the low $(Gd/Yb)_N$ ratios of two-mica granites (3.04–3.57; Fig. 7C).

Typical leucogranitic melts can be produced by: (1) water-fluxed melting induced by the introduction of a H_2O-rich fluid phase; and (2) fluid-absent dehydration melting of muscovite, biotite, and hornblende (Clemens, 2006; Reichardt and Weinberg, 2012). Niobium and Ta are considered to partition similarly throughout the magmatic evolution of peraluminous granites, except during fractionation of Ti-rich minerals and/or interaction with late magmatic fluids (Ballouard et al.,

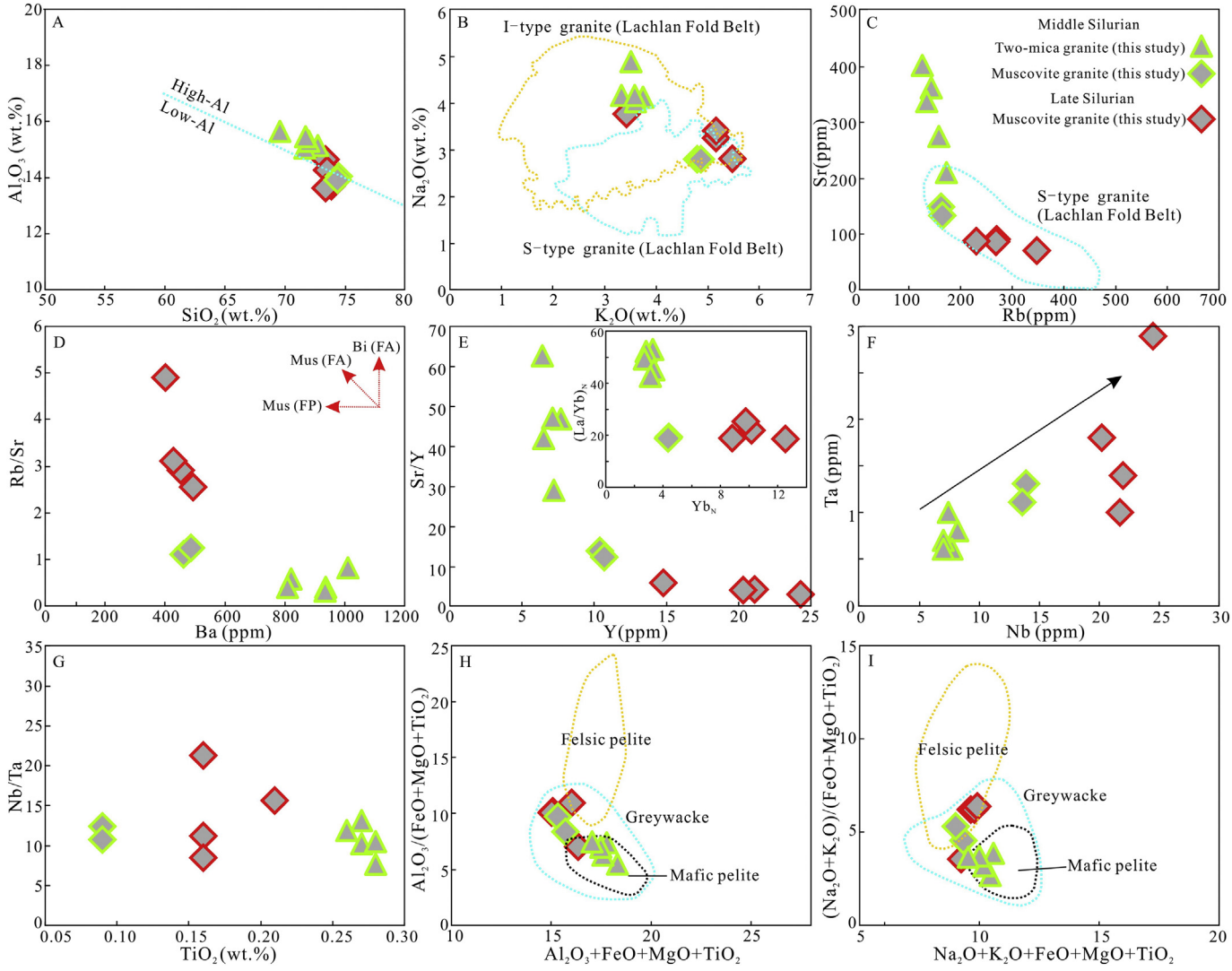

Fig. 10. Geochemical comparisons for the Silurian two-mica and muscovite granites: (A) Al_2O_3 vs. SiO_2 diagram (boundary between the high-Al and low-Al is from Frost et al., 2016); (B–C) plots of Na_2O vs. K_2O and Sr vs. Rb (the ranges of I- and S-type granites in Lachan Fold Belt are from Chappell and White, 2001); (D) Rb/Sr vs. Ba plots, experimental trends for fluid-absent (FA) melting, dominated by biotite (Bi) and muscovite (Mus), and fluid-present (FP) melting, dominated by muscovite, are shown by the small red vectors; (E) Sr/Y vs. Y and $(La/Yb)_N$ vs. Yb_N diagrams; (F–G) plots of Ta vs. Nb and Nb/Ta vs. TiO_2; (H–I) discrimination diagrams of crustal sources for leucogranites (Inger and Harris, 1993; Patiño Douce, 1999).

2016; Linnen and Keppler, 1997). The Silurian two-mica and muscovite granites have different TiO_2 contents and similar Nb/Ta values (Fig. 10G); this indicates that the different Nb and Ta contents (Fig. 10F) are a consequence of differences in the amounts of micas involved in crustal melting, rather than rutile fractionation and hydrothermal alteration (Gao et al., 2017). Niobium and Ta can partition into melts generated by fluid-absent melting, so the low Nb and Ta contents of the two-mica granites (Fig. 10F) indicate that these granites formed by fluid-present melting (Gao et al., 2017; Harris et al., 1995). This inference is supported by the following observations: (1) extremely low Rb/Sr ratios (0.31–0.81; Fig. 10C, D), which typically reflect fluid-present melting (Rb/Sr < 2) rather than dehydration melting (Rb/Sr > 2) (Inger and Harris, 1993); and (2) fluid-present melting of crustal rocks can produce trondhjemitic melts with low K_2O contents, which is consistent with the low K_2O contents (3.33–3.74 wt%), high Na_2O contents (4.01–4.88 wt%), and Na_2O/K_2O ratios (1.10–1.39) of the two-mica granites (Conrad et al., 1988; Gardien et al., 2000; Fig. 10B).

The leucogranites have been attributed to melting of a range of crustal rocks, including amphibolites, metasedimentary rocks, and silicic orthogneiss (Wang et al., 2017; Zeng et al., 2011). However, metasediments can be excluded because metasediment-derived melts have Rb/Sr ratios greater than one (Zhang et al., 2004), which is significantly higher than the Rb/Sr ratios of the two-mica granites (0.31–0.81). This inference is also consistent with the low initial Sr isotope ratios of 0.70715 to 0.70804, and high $\varepsilon_{Nd}(t)$ values of −3.14 to −2.02. The high Sr (210–401 ppm) and Al_2O_3 (15.02–15.66 wt%) contents (Fig. 10A, C) might reflect plagioclase melting in the source of the two-mica granites and suppression of plagioclase crystallization by high water contents during the early evolution of the magma (Müntener et al., 2001). The low Y and HREE contents and small Eu anomaly (Figs. 7C, 10E) imply retention of HREE-enriched minerals (garnet and hornblende) in the source (Frost et al., 2016). However, as noted above, garnet is not a residual phase. Therefore, we infer that the restite included large amounts of hornblende. This unusual situation has been replicated by partial melting experiments. Beard and Lofgren (1991) conducted water-fluxed melting experiments on metamorphosed basalts and andesites, that produced hornblende-rich, plagioclase-poor residues and strongly peraluminous melts with high Al_2O_3, LREE, and Sr contents, low K_2O, HREE, and Y contents, and negligible Eu anomalies (Figs. 7C, 10A–E; Beard and Lofgren, 1991; Frost et al., 2016). These characteristics resemble those of the two-mica granites. The Sr-Nd isotopic compositions of the two-mica granites are similar to those of the early–middle Silurian diorites and quartz diorites, but dramatically different from those of the Qinling Group gneisses of the NQT (Fig. 8A, B), indicating that they are derived from water-present melting of early–middle Silurian metamorphosed igneous rocks sourced from enriched mantle.

6.3.2.2. Muscovite granite. Diagrams that discriminate amongst crustal sources (Fig. 10H, I) indicate that the middle Silurian muscovite granites are derived from (meta-)graywackes, consistent with their evolved Sr–Nd–Hf isotopic compositions ($(^{87}Sr/^{86}Sr)_i$ = 0.71285–0.71334; $\varepsilon_{Nd}(t)$ = −3.63 to −3.49; $\varepsilon_{Hf}(t)$ = −6.61 to −0.44) and predominance of biotite–plagioclase gneisses within the crustal rocks of the NQT. Trends in Rb, Sr, Ba, Nb, and Ta are also consistent with water-present melting for the following reasons.

(1) Melts generated by fluid-present and dehydration melting have Rb/Sr ratios of <2 and > 2, respectively, as noted above (Inger and Harris, 1993), and fluid-present melting of sedimentary rocks generates melts with relatively low Rb/Sr ratios (~2; Harris and Inger, 1992). Therefore, we infer that the relatively low Rb/Sr ratios (1.11–1.24) of the muscovite granites reflect water-present partial melting.
(2) Constant Rb/Sr ratios with decreasing Ba content are attributed to water-present partial melting (Fig. 10D; Inger and Harris, 1993).
(3) Relatively low Nb (13.6–13.9 ppm) and Ta (1.10–1.30 ppm) contents (Fig. 10F) indicate water-present melting (Section 6.3.2.1; Gao et al., 2017).

In summary, we infer that the middle Silurian diorites and quartz diorites formed by crustal assimilation and fractional crystallization of basaltic partial melts of a pre-existing mantle source that had been altered by slab-derived hydrous fluids, and that was subsequently modified by slab-melts. The two-mica and muscovite granites derive from water-present melting of early–middle Silurian metamorphosed igneous rocks sourced from enriched mantle and (meta-)graywackes, respectively.

6.4. Petrogenesis of the late Silurian intrusions

6.4.1. Quartz diorites

The late Silurian quartz diorites have $(^{87}Sr/^{86}Sr)_i$ ratios of 0.70473 to 0.70505, $\varepsilon_{Nd}(t)$ values of 1.39 to 1.83, and $\varepsilon_{Hf}(t)$ values of 7.73 to 11.2, which differ from the isotopic characteristics of Qinling Group gneisses of the NQT (Fig. 8A, B) and preclude their derivation from crustal materials. Some features of their geochemistry are similar to those of the early–middle Silurian diorites and quartz diorites, such as high Ba and Sr contents (585–751 ppm and 297–399 ppm, respectively) and low Rb contents (74.8–99.9 ppm), and negative Nb and Ta anomalies (Figs. 7F, 9A), consistent with derivation from enriched mantle. However, the Sr–Nd–Hf isotope compositions are more depleted than those of the early and middle Silurian diorites and quartz diorites (Fig. 8A, B), indicating that the depleted asthenosphere mantle was a major contributor to the late Silurian quartz diorites. The low Mg numbers (Mg# = 46.7–48.4) and the mild negative Eu anomaly (Eu/Eu* = 0.57–0.66) probably reflect fractionation of plagioclase and mafic minerals. Crustal xenoliths and xenocrystic zircons are absent in these rocks, indicating that crustal assimilation was negligible.

6.4.2. Granites

The late Silurian granites have low K/Rb ratios (165–262) and strong negative Eu anomalies (Fig. 7E), consistent with the characteristics of moderately to highly fractionated granites (Fig. 11A). Moderate to high degrees of fractionation can produce variable element concentrations, especially the HFSEs and 10000*Ga/Al (Fig. 11F–J), which are used to discriminate A-type granites from other granites. Therefore, only the less-fractionated granites (SiO_2 < 70 wt%) are considered to provide a reliable record of the composition of the initial parental magma and information on genetic type. The granites with the lowest SiO_2 contents show an affinity with A-type granite (Fig. 11K, L). Their $\varepsilon_{Hf}(t)$ values are intermediate between those of the early–middle and late Silurian diorites and quartz diorites (Fig. 8B), which indicate that they formed by anatexis of juvenile mafic lower crust. Details of crystal fractionation can be inferred, based on the following: (1) decreasing MgO, CaO, Na_2O, P_2O_5, Sr, Nb, and Ce contents with increasing SiO_2 contents (Fig. 11B–G) imply fractionation of mafic minerals, plagioclase, and accessory minerals, such as apatite; (2) fractionation of rock-forming minerals can cause weak Zr/Hf variation, while zircon fractionation reduces Zr/Hf ratios significantly (Münker et al., 2004). Therefore, the decreasing Zr content and Zr/Hf ratio with increasing SiO_2 content (Fig. 11I) indicates extensive zircon fractionation; and (3) decreasing Nb and Ta concentrations and sharply elevated Nb/Ta ratios of granites with increasing SiO_2 (Fig. 11G, J) probably reflect fractionation of rutile and ilmenite, because these minerals fractionate Nb from Ta ($D_{Nb/Ta}$ < 1; Linnen and Keppler, 1997).

6.4.3. Muscovite granite

Diagrams that discriminate amongst crustal sources (Fig. 10H, I) and the evolved isotopic composition of the granite ($(^{87}Sr/^{86}Sr)_i$ = 0.71044–0.71126, $\varepsilon_{Nd}(t)$ = −5.35 to −4.74), indicate that the

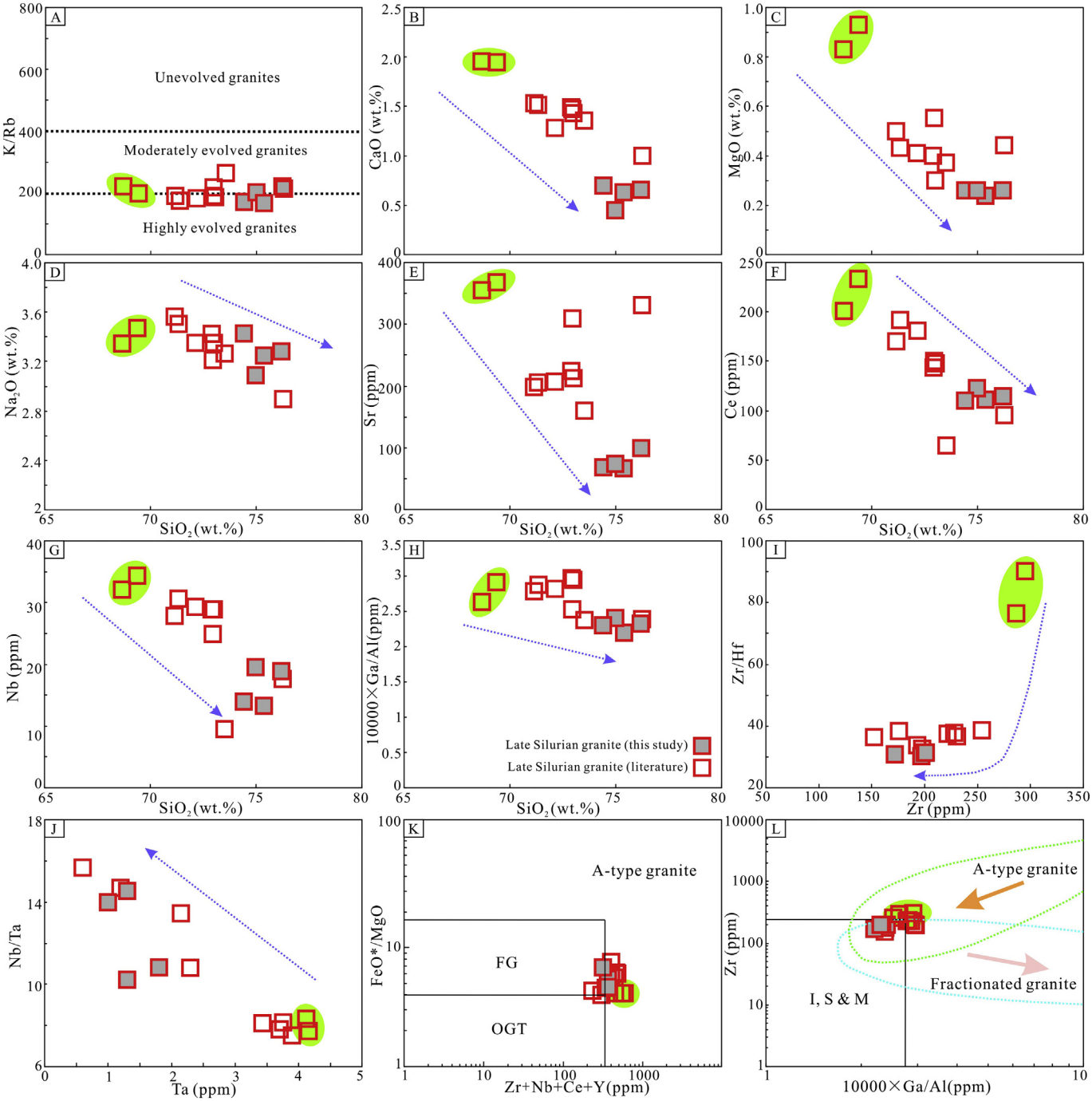

Fig. 11. Geochemical diagrams for the late Silurian granites: (A) plot of K/Rb vs. SiO_2; (B–I) Harker-type diagrams; (J–K) bivariate trace element diagrams; (L–O) A-type granite discrimination diagrams (Blevin, 2004; Whalen et al., 1987). The green shadow represents the samples with the least SiO_2 contents (<70 wt%).

muscovite granites derive from (meta-)graywackes. The strong negative Eu anomaly ($Eu/Eu^* = 0.21–0.31$; Fig. 7E) is consistent with vapor-absent dehydration melting of sedimentary rocks (Harris and Inger, 1992), and is also consistent with their high Nb and Ta contents (Fig. 10F) and Rb/Sr ratios of 2.54–4.90 (Gao et al., 2017). During fluid-absent dehydration melting, the main hydrous reacting phases are muscovite, biotite, and hornblende (Weinberg and Hasalová, 2015). Experimental petrology has shown that hornblende dehydration melting reactions require high melting temperatures (850–900 °C), and can yield dioritic to granodioritic and peralkaline to metaluminous melts with low K/Na ratios (Wolf and Wyllie, 1994). These features are not observed in the muscovite granites ($SiO_2 = 73.42–73.92$ wt%, $K_2O/Na_2O = 0.91–1.94$, A/CNK = 1.07–1.31). Melts produced by muscovite dehydration melting have extremely high Rb/Sr ratios (>5) and low Ti, Ba, Mg, and LREE contents, whereas biotite dehydration melting produces lower Rb/Sr ratios (<4.5) and higher Ti, Mg, Ba, and LREE concentrations (Inger and Harris, 1993). The late Silurian muscovite granites have moderate Rb/Sr ratios (2.54–4.90), and high TiO_2 (0.16–0.21 wt%), MgO (0.14–0.28 wt%), Ba (401–494 ppm), and LREE (155–238 ppm) contents, which are consistent with derivation by biotite dehydration melting of (meta-)graywackes.

In summary, we infer that the late Silurian quartz diorites formed by fractionation of basaltic partial melts of enriched mantle, with a large contribution from depleted asthenospheric mantle. The A-type granites

were generated by anatexis of juvenile mafic lower crust and subsequent fractional crystallization. The muscovite granites formed by biotite dehydration melting of (meta-) graywackes.

6.5. Geodynamic implications

There is consensus that northward subduction of the Shangdan Ocean began before c. 500 Ma (Fig. 12A; Dong et al., 2011; Wang et al., 2014), but the tectonic evolution of the Qinling Orogenic Belt from c. 500 to c. 400 Ma remains unresolved. The origins of three early Paleozoic magmatic flare-ups in the western NQT provide new insights into this part of the history of the Qinling Orogenic Belt. Our tectonic interpretation is based mainly on geochemical data and the petrogenesis of the three magmatic flare-ups; further work is necessary to produce a detailed and accurate reconstruction of the tectonic configuration.

6.5.1. Slab rollback at c. 448–434 Ma

Late Ordovician–early Silurian arc-type mafic intrusions of the western NQT, such as the Hualingou, Yuanyangzhen, and Baihua mafic intrusions, and volcanic rocks represented by the Caotangou Group, have consistent zircon U-Pb ages of 456–435 Ma (Li, 2008; Pei et al., 2007b; Ren et al., 2018). Furthermore, a suite of bimodal volcanic rocks with ages of 448–443 Ma, inferred to have formed in a back-arc basin setting, are recognized in the Chenjiahe–Hongtubao area of the western NQT (Li, 2008; Fig. 2). Therefore, we propose that northward subduction of the Shangdan Ocean continued until the early Silurian and that the early Silurian pulsed intermediate–silicic intrusive rocks were produced in a subduction setting at 441–434 Ma (Fig. 12B). It has been suggested that bimodal magmatism in back-arc basin settings reflects asthenospheric decompression melting caused by slab rollback (Toksöz and Bird, 1977). The early Silurian magmatism (441–434 Ma) is slightly later than the back-arc basin magmatism (448–443 Ma), so we infer that the early Silurian flare-up was also controlled by slab rollback and associated asthenospheric convection. In this scenario, slab rollback initiated asthenospheric decompression melting in the mantle wedge and generated back-arc basin magmatism. Subsequently, asthenospheric convection induced partial melting of enriched mantle that had interacted with slab-derived fluids and produced basaltic magma that evolved into the early Silurian diorites and quartz diorites by fractional crystallization. Slab rollback and its consequences strongly increased the geothermal gradient of the lower crust, which formed the early Silurian granites (Fig. 12B).

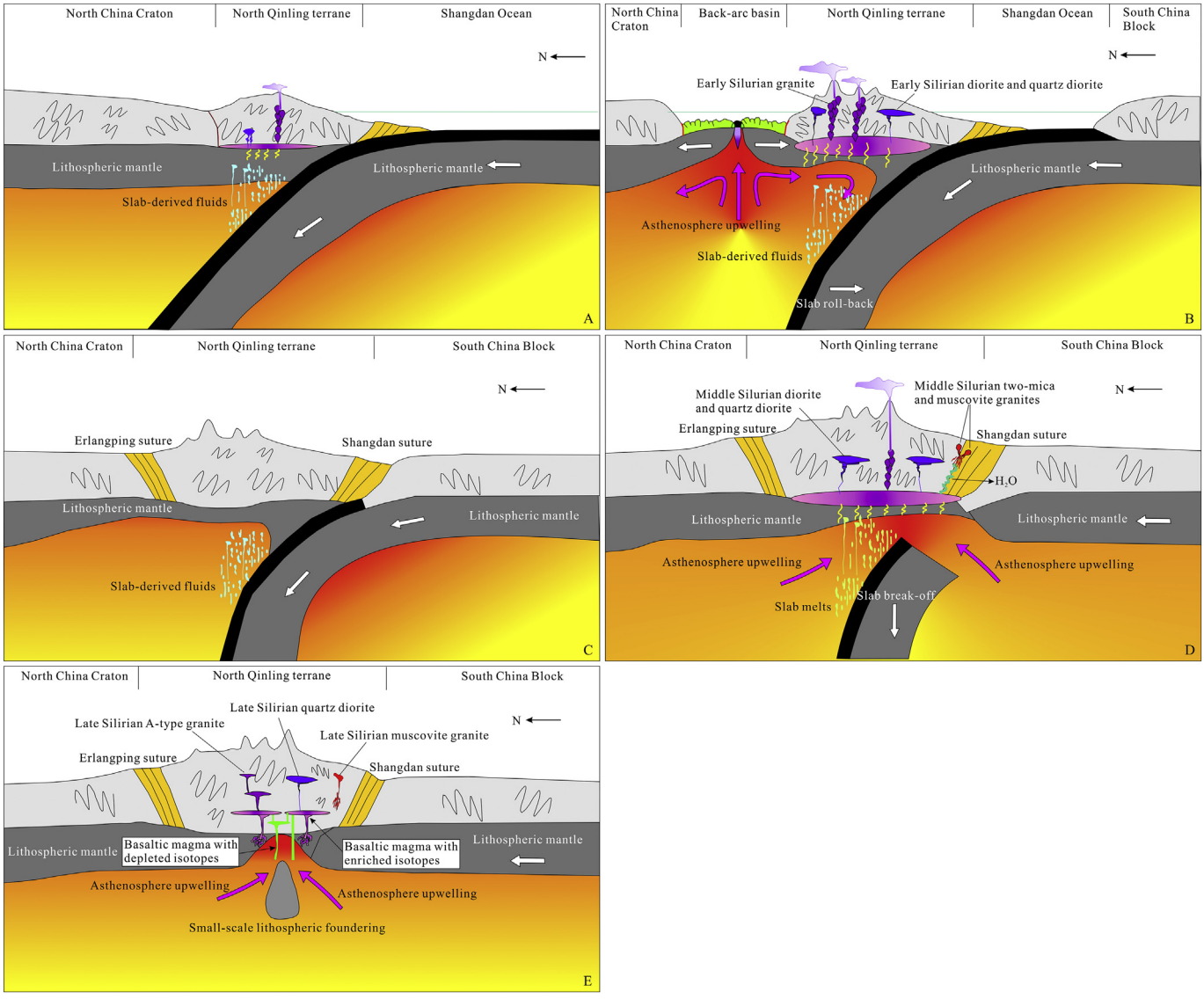

Fig. 12. Cartoons illustrating early Paleozoic tectonic evolution of the Qinling Orogenic Belt: (A) northward subduction of the Shangdan Ocean; (B) early Silurian slab rollback; (C) initial continental collision at c. 433 Ma; (D) middle Siurian slab break-off; (E) late Silurian small-scale lithospheric foundering in the post-collisional setting.

6.5.2. Initial continental collision at c. 433 Ma

The middle Silurian flare-up is characterized by two-mica (430 Ma) and muscovite granites (423 Ma) related to crustal melting. These leucogranites intrude the Shangdan suture zone, consistent with continental collision before c. 430 Ma. Slab rollback in an oceanic subduction setting occurred at 448–434 Ma, which constrains continental collision between the NCC and SCB to c. 434–430 Ma in the Qinling Orogenic Belt. The Qinling Group near our research area underwent granulite-facies metamorphism at 433–426 Ma (Mao et al., 2017), so we infer that the initial continental collision of the NCC and SCB probably occurred at c. 433 Ma (Fig. 12C).

6.5.3. Slab break-off at c. 430–423 Ma

In contrast to the early Silurian diorites and quartz diorites, which were derived from the mantle wedge that interacted with slab-derived hydrous fluids, the middle Silurian diorites and quartz diorites originated from a mantle source that had interacted with hydrous fluids and that was altered subsequently by slab-melts. This is consistent with interaction of the mantle with adakitic partial melts of the subducted basaltic slab at c. 429–425 Ma. The middle Silurian two-mica and muscovite granites formed by water-present melting of crustal rocks within the shear zone that represents the Shangdan suture zone, which indicates that aqueous fluids induced localized fluid-present melting of

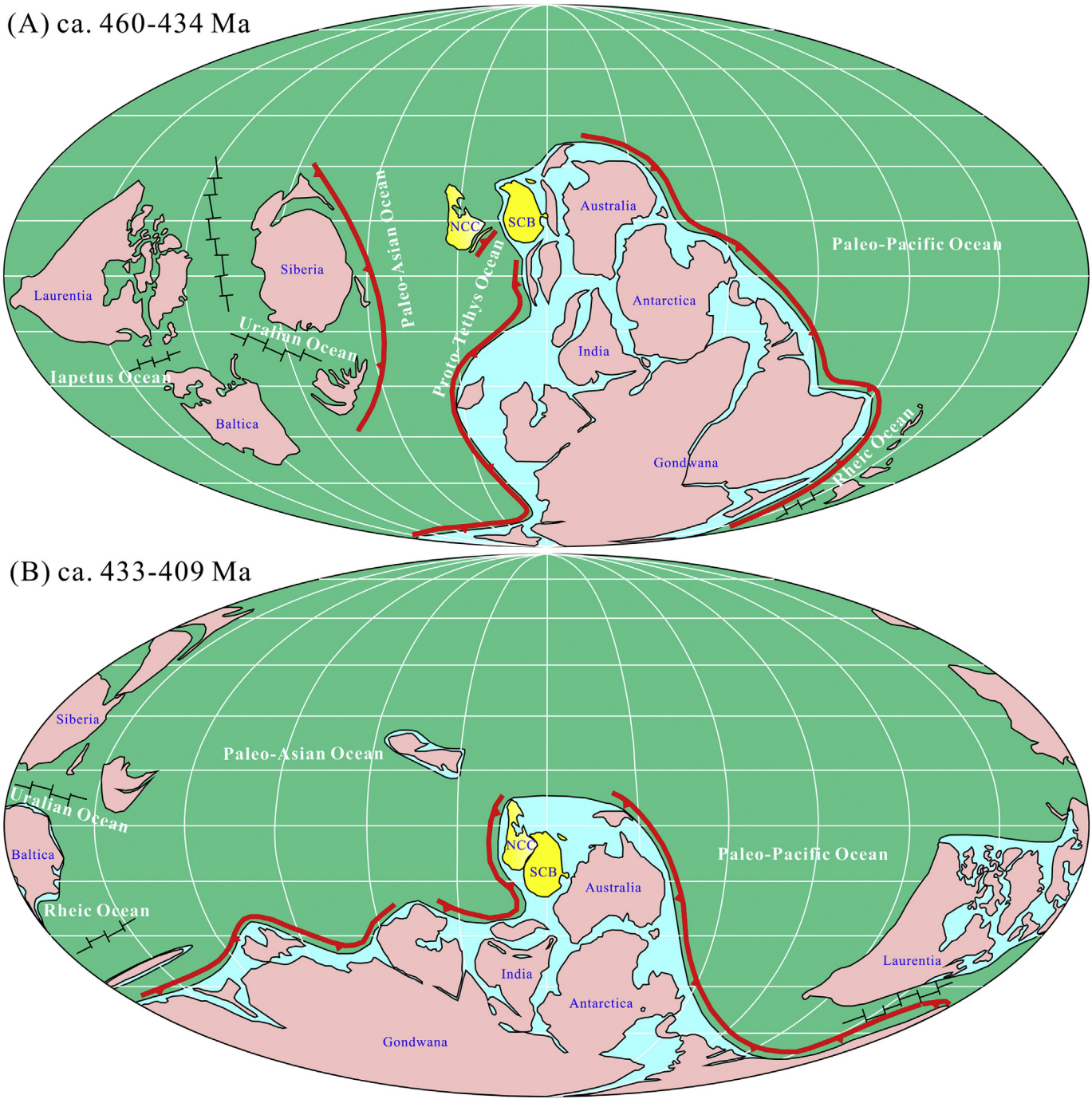

Fig. 13. Cartoons showing convergence of the NCC and SCB on the northern margin of Gondwana. Modified after Huang et al., 2018; Zhao et al., 2018.

crustal materials within the shear zone. This indicates that the active shear zone provided a channel for fluid migration with locally low fluid pressures that attracted fluids on a regional scale (Mancktelow, 2006; Weinberg and Hasalová, 2015). In general, enriched mantle that has interacted with slab–related fluids or hydrous melts from the subduction zone contains large amount of fluids, and partial melts of this material can transfer large amounts of aqueous fluids into the middle–upper crust along shear zones (Vernon and Clarke, 2008). Therefore, a significant geodynamic change, possibly related to the opening of a slab window, occurred in the Qinling Orogenic Belt during the middle Silurian continental collision, and this led to partial melting of the basaltic slab and enriched lithospheric mantle and water-present melting of crustal material (Fig. 12D). Slab break-off that occurs just a few millions of years after continental collision can be induced by density contrasts at the intersection of the continental and oceanic slabs (van de Zedde and Wortel, 2001). The age of middle Silurian magmatism in the Qinling Orogenic Belt (430–423 Ma) is slightly younger than that of the initial continental collision (c. 433 Ma; Fig. 12D), as expected for slab break-off.

6.5.4. Post-collisional small-scale lithospheric foundering at c. 415–409 Ma

Involvement of depleted asthenospheric mantle in the late Silurian quartz diorites indicates high flow rates within the asthenospheric mantle. Furthermore, the A-type granites derived by anatexis of juvenile mafic lower crust reflect an extensional geodynamic setting. The late Silurian muscovite granites with leucogranite affinities are commonly interpreted as a record of continental collision (Wu et al., 2015). Indeed, most leucogranites are closely related to delamination of thickened continental crust in post-collisional settings, and minor leucogranites form during continental collision and subsequent slab break-off (Wu et al., 2015). Given that slab break-off occurred at 430–423 Ma in the Qinling Orogenic Belt, delamination of thickened crust might have caused extension during the late Silurian. Continued continental compression from c. 433 to c. 415 Ma would cause shortening and thickening of the continental crust and underlying lithospheric mantle to produce a high-density lithospheric root (eclogitic root) that protruded into the asthenosphere (Houseman and Molnar, 1997). Delamination can manifest as large-scale lithospheric delamination or Rayleigh–Taylor convective instabilities (Yi et al., 2018). The weak late Silurian magmatism (Fig. 2) is inconsistent with large-scale delamination. Rayleigh–Taylor convective instabilities occur when the high-density eclogitic root falls into the asthenosphere and initiates asthenosphere upwelling. If the amount of high-density material is small then foundering is slow and the resultant asthenosphere upwelling and magmatism are limited (Drew et al., 2009). Therefore, the low volumes of late Silurian magmatism were probably caused by small-scale foundering of high-density lithospheric root (Fig. 12E).

6.6. New constraints on convergence of the North China Craton and South China Block on the northern Gondwana margin

There have been numerous investigations of early Paleozoic convergence of the NCC and SCB on the northern Gondwana margin (Huang et al., 2018; Yu et al., 2015; Zhao et al., 2018). However, this process is still debated because of the paucity of mid-Paleozoic paleomagnetic data, and the late Ordovician to early Carboniferous sedimentary hiatus in the NCC. Zhao et al. (2018) inferred that the NCC drifted northeastward to collide with the SCB on the northern Gondwana margin at 500–460 Ma, whereas Yu et al. (2015) inferred that the NCC accreted onto the SCB on the northern Gondwana margin at 440–400 Ma. Huang et al. (2018) acknowledged that the NCC and SCB drifted towards the northern Gondwana margin, but challenged the notion of an early Paleozoic collision between the NCC and SCB. The Qinling Orogenic Belt is a consequence of the early Paleozoic convergence of the NCC and SCB, so its Paleozoic tectonic evolution might provide insights into the configuration of Gondwana.

The convergence of the SCB and Gondwana have been inferred to have occurred at c. 540 Ma and c. 460 Ma. These dates are supported by the early Paleozoic metamorphic ages (460–420 Ma) of the Huanan Orogen in the SCB, and fauna, flora, paleomagnetic, and stratigraphic data, respectively (Li et al., 2010b; Metcalfe, 2013; Yu et al., 2015; Zhao et al., 2018). However, this uncertainty does not affect our conclusion, which is that the SCB was a part of Gondwana after c. 460 Ma (Fig. 13A). The NCC shares early Paleozoic faunal assemblages and paleomagnetic latitudinal ranges with the SCB and Australia (Huang et al., 2008; Metcalfe, 2013), indicating that the NCC was located on the northern Gondwana margin and was closely linked to Australia and the SCB during the Ordovician. Furthermore, previous studies have shown that the Ordovician Iapetus and Proto-Tethys oceans separated Gondwana from other continental blocks and the Proto-Tethys Ocean separated Gondwana/SCB from the NCC (Stampfli and Borel, 2002; Fig. 13A). As discussed above, northward subduction of the Shangdan Ocean occurred at c. 500–434 Ma, so the NCC and SCB were still separated by the Proto-Tethys Ocean after convergence of the SCB and Gondwana (Fig. 13A). Moreover, early Paleozoic igneous, metamorphic, and paleontological records of the western NQT show that the Proto-Tethys Ocean began to close at c. 433 Ma, so amalgamation of the NCC with the northern Gondwana margin probably occurred at c. 433 Ma (Fig. 13B). Based on these lines of evidence, amalgamation of the NCC and SCB onto the northern Gondwana margin was probably completed by the early Silurian (c. 433 Ma).

7. Conclusions

(1) The early Silurian (c. 441–434 Ma) pulse of diorite–quartz diorite–granite magmatism is closely related to slab rollback.
(2) A middle Silurian (c. 430–423 Ma) high-flux magmatic pulse related to slab break-off formed diorites, quartz diorites, and leucogranites (two-mica and muscovite granites).
(3) Late Silurian (c. 415–409 Ma) quartz diorites, A-type granites, and muscovite granites formed in response to small-scale lithospheric foundering in a post-collisional setting.
(4) Amalgamation of the NCC and SCB with the northern Gondwana margin was probably completed by c. 433 Ma.

Supplementary data to this article can be found online at https://doi.org/10.1016/j.lithos.2020.105833.

Declaration of Competing Interest

The authors declare that they have no known competing financial interest or personal relationships that could have appeared to influence the work reported in this paper.

Acknowledgement

We are very grateful to the Editor Prof. Greg Shellnutt, Prof. Chang Whan Oh, Prof. Scott A. Whattam and an anonymous reviewer for their constructive comments and suggestions, which greatly improved manuscript quality. This study was funded by the National Natural Science Foundation of China (Grant No. 41772065), China Postdoctoral Science Foundation (Grant No. 2020M672852) and the collaborative project between the Sino Shaanxi Nuclear Industry Group and Guangzhou Institute of Geochemistry, Chinese Academy of Sciences. Field assistance was provided by the brigade NO. 211 of Sino Shaanxi Nuclear Industry Group. This is contribution No. IS-2905 from GIGCAS.

References

Annen, C., Blundy, J., Sparks, R., 2006. The genesis of intermediate and silicic magmas in deep crustal hot zones. J. Petrol. 47 (3), 505–539.

Ballouard, C., Poujol, M., Boulvais, P., Branquet, Y., Tartese, R., Vigneresse, J., 2016. Nb–Ta fractionation in peraluminous granites: a marker of the magmatic–hydrothermal transition. Geology 44 (7), 231–234.
Beard, J.S., Lofgren, G.E., 1991. Dehydration melting and water–saturated melting of basaltic and andesitic greenstones and amphibolites at 1, 3, and 6.9 kb. J. Petrol. 32 (2), 365–401.
Blevin, P.L., 2004. Redox and compositional parameters for interpreting the granitoid metallogeny of Eastern Australia: implications for gold-rich ore systems. Resour. Geol. 54, 241–252.
Chappell, B.W., White, A.J.R., 2001. Two contrasting granite types: 25 years later. Aust. J. Earth Sci. 48 (4), 489–499.
Clemens, J.D., 2006. Melting of the continental crust: fluid regimes, melting reactions, and source–rock fertility. In: Brown, M., Rushmer, T. (Eds.), Evolution and Differentiation of the Continental Crust. Cambridge University Press, Cambridge, UK, pp. 297–331.
Clemens, J.D., Stevens, G., 2012. What controls chemical variation in granitic magmas? Lithos 134–135, 317–329.
Conrad, W.K., Nicholls, I.A., Wall, V.J., 1988. Water–saturated and –undersaturated melting of metaluminous and peraluminous crustal compositions at 10 kbar: evidence for the origin of silicic magmas in the Taupo volcanic zone, New Zealand, and other occurrences. J. Petrol. 29, 765–803.
de Silva, S.L., Riggs, N.R., Barth, A.P., 2015. Quickening the pulse: fractal tempos in continental arc magmatism. Elements 11 (2), 113–118.
DeCelles, P.G., Ducea, M.N., Kapp, P., Zandt, G., 2009. Cyclicity in Cordilleran orogenic systems. Nat. Geosci. 2 (4), 251–257.
Dong, Y.P., Zhang, G.W., Hauzenberger, C., Neubauer, F., Yang, Z., Liu, X.M., 2011. Paleozoic tectonics and evolutionary history of the Qinling orogen: evidence from geochemistry and geochronology of ophiolite and related volcanic rocks. Lithos 122 (1–2), 39–56.
Dong, Y.P., Liu, X.M., Neubauer, F., Zhang, G.W., Tao, N., Zhang, Y.G., Zhang, X.N., Li, W., 2013. Timing of Paleozoic amalgamation between the North China and South China Blocks: evidence from detrital zircon U–Pb ages. Tectonophysics 586 (26), 173–191.
Dong, Y.P., Yang, Z., Liu, X.M., Sun, S.S., Li, W., Cheng, B., Zhang, F.F., Zhang, X.N., He, D.F., Zhang, G.W., 2016. Mesozoic intracontinental orogeny in the Qinling Mountains, central China. Gondw. Res. 30, 144–158.
Drew, S.T., Ducea, M.N., Schoenbohm, L.M., 2009. Mafic volcanism on the Puna Plateau, NW Argentina: implications for lithospheric composition and evolution with an emphasis on lithospheric foundering. Lithosphere 1 (5), 305–318.
Fowler, M.B., Kocks, H., Darbyshire, D.P.F., Greenwood, P.B., 2008. Petrogenesis of high Ba–Sr plutons from the Northern Highlands Terrane of the British Caledonian Province. Lithos 105 (1–2), 129–148.
Frost, B.R., BArnes, C.G., Collins, W.J., ArCulus, R.J., Ellis, D.J., Frost, C.D., 2001. A geochemical classification for granitic rocks. J. Petrol. 42 (11), 2033–2048.
Frost, C.D., Swapp, S.M., Frost, B.R., Blasi, L.F., Fitz–Gerald, D.B., 2016. Leucogranites of the Teton Range, Wyoming: a record of Archean collisional orogeny. Geochim. Cosmochim. Acta 185, 528–549.
Gao, L.E., Zeng, L.S., Asimow, P.D., 2017. Contrasting geochemical signatures of fluid–absent versus fluid–fluxed melting of muscovite in metasedimentary sources: the Himalayan leucogranites. Geology 45 (1), 39–42.
Gardien, V., Thompson, A.B., Ulmer, P., 2000. Melting of biotite + plagioclase + quartz gneisses: the role of H_2O in the stability of amphibole. J. Petrol. 41 (5), 651–666.
Harris, N., Ayres, M., Massey, J., 1995. Geochemistry of granitic melts produced during the incongruent melting of muscovite: Implication for the extraction of Himalayan leucogranite magmas. J. Geophys. Res. Solid Earth 100 (B8), 15767–15777.
Harris, N., Inger, S., 1992. Trace element modelling of pelite-derived granites. Contrib. Mineral. Petrol. 110, 46–56.
Houseman, G.A., Molnar, P., 1997. Gravitational (Rayleigh–Taylor) instability of a layer with non–linear viscosity and convective thinning of continental lithosphere. Geophys. J. Int. 128 (1), 125–150.
Huang, F., He, Y.S., 2010. Partial melting of the dry mafic continental crust: Implications for petrogenesis of C–type adakites. Chin. Sci. Bull. 55 (13), 1255–1267 (in Chinese).
Huang, B.C., Zhou, Y.X., Zhu, R.X., 2008. Discussion on Phanerozoic evolution and formation of continental China, based on paleomagnetic studies. Earth Sci. Front. 15 (3), 348–359 (in Chinese with English abstract).
Huang, B.C., Yan, Y.G., Piper, J.D.A., Zhang, D.H., Yi, Z.Y., Yu, S., Zhou, T.H., 2018. Paleomagnetic constraints on the paleogeography of the East Asian blocks during Late Paleozoic and Early Mesozoic times. Earth Sci. Rev. 186, 8–36.
Inger, S., Harris, N., 1993. Geochemical constraints on leucogranite magmatism in the Langtang Valley, Nepal Himalaya. J. Petrol. 34 (2), 345–368.
Li, W.Y., 2008. Geochronology and Geochemistry of the Ophiolites and Island–arc–type Igneous Rocks in the Western Qinling Orogeny and the Eastern Kunlun Orogeny: Implications for the Evolution of the Tethyan Ocean. PhD Thesis. University of Science and Technology of China, Hefei, pp. 1–154 (in Chinese with English abstract).
Li, X.H., Long, W.G., Li, Q.L., Liu, Y., Zheng, Y.F., Yang, Y.H., Chamberlain, K.R., Wan, D.F., Guo, C.H., Wang, X.C., Tao, H., 2010a. Penglai zircon megacrysts: a potential new working reference material for microbeam determination of Hf–O isotopes and U–Pb age. Geostand. Geoanal. Res. 34 (2), 117–134.
Li, Z.X., Li, X.H., Wartho, J.A., Clark, C., Li, W.X., Zhang, C.L., Bao, C.M., 2010b. Magmatic and metamorphic events during the early Paleozoic Wuyi–Yunkai orogeny, southeastern South China: new age constraints and pressure–temperature conditions. Geol. Soc. Am. Bull. 122 (5–6), 772–793.
Li, Y., Yang, J.S., Dilek, Y., Zhang, J., Pei, X.Z., Chen, S.Y., Xu, X.Z., Li, J.Y., 2015. Crustal architecture of the Shangdan suture zone in the early Paleozoic Qinling orogenic belt, China: record of subduction initiation and backarc basin development. Gondw. Res. 27 (2), 733–744.
Linnen, R.L., Keppler, H., 1997. Columbite solubility in granitic melts: Consequences for the enrichment and fractionation of Nb and Ta in the Earth's crust. Contrib. Mineral. Petrol. 128 (2–3), 213–227.
Liu, C.J., 2013. Study on Material Composition, Tectonic Evolution and Transformation at the Conjunction of Qinling and North Qilian Orogen. MS Dissertation. Chang'an University, Xi'an, pp. 1–109 (in Chinese with English abstract).
Liu, L., Liao, X.Y., Wang, Y.W., Wang, C., Santosh, M., Yang, M., Zhang, C.L., Chen, D.L., 2016. Early Paleozoic tectonic evolution of the North Qinling Orogenic Belt in Central China: insights on continental deep subduction and multiphase exhumation. Earth Sci. Rev. 159, 58–81.
Mancktelow, N.S., 2006. How ductile are ductile shear zones? Geology 34 (5), 345–348.
Mao, X.H., Zhang, J.X., Yu, S.Y., Li, Y.S., Yu, X.X., Lu, Z.L., 2017. Early Paleozoic granulite–facies metamorphism and anatexis in the Northern West Qinling orogen: monazite and zircon U–Pb geochronological constraints. Chin. Sci. Bull. 60 (5), 943–957.
Martin, H., Smithies, R.H., Rapp, R., Moyen, J.F., Champion, D., 2005. An overview of adakite, tonalite–trondhjemite–granodiorite (TTG), and sanukitoid: relationships and some implications for crustal evolution. Lithos 79 (1–2), 1–24.
Metcalfe, I., 2013. Gondwana dispersion and Asian accretion: tectonic and palaeogeographic evolution of eastern Tethys. J. Asian Earth Sci. 66, 1–33.
Moyen, J.F., Martin, H., 2012. Forty years of TTG research. Lithos 148, 312–336.
Münker, C., Wörner, G., Yogodzinski, G., Churikova, T., 2004. Behaviour of high field strength elements in subduction zones: constraints from Kamchatka–Aleutian arc lavas. Earth Planet. Sci. Lett. 224 (3–4), 275–293.
Müntener, O., Kelemen, P.B., Grove, T.L., 2001. The role of H_2O during crystallization of primitive arc magmas under uppermost mantle conditions and genesis of igneous pyroxenites: an experimental study. Contrib. Mineral. Petrol. 141 (6), 643–658.
Patiño Douce, A.E., 1999. What do experiments tell us about the relative contributions of crust and mantle to the origin of granitic magmas? Geol. Soc. Lond. Spec. Publ. 168 (1), 55–75.
Pei, X.Z., Sun, R.Q., Ding, S.P., Liu, H.B., Li, Z.C., Liu, Z.Q., Meng, Y., 2007a. LA–ICP–MS zircon U–Pb dating of the Yanjiadian diorite in the eastern Qilian Mountains and its geological significance. Geol. China 34 (1), 8–16 (in Chinese with English abstract).
Pei, X.Z., Ding, S.P., Zhang, G.W., Liu, H.B., Li, Z.C., Li, G.Y., Liu, Z.Q., Meng, Y., 2007b. The LA–ICP–MS zircon U–Pb ages and geochemistry of the Baihua basic igneous complexes in Tianshui area of West Qinling. Sci. China Ser. D 50 (2), 264–276.
Reichardt, H., Weinberg, R.F., 2012. Hornblende chemistry in meta– and diatexites and its retention in the source of leucogranites: an example from the Karakoram Shear Zone, NW India. J. Petrol. 58 (6), 1287–1318.
Ren, L., Liang, H.Y., Bao, Z.W., Zhang, J., Li, K.X., Huang, W.T., 2018. The petrogenesis of early Paleozoic high–Ba–Sr intrusions in the North Qinling terrane, China, and tectonic implications. Lithos 314–315, 534–550.
Ren, L., Bao, Z.W., Zhang, J., Li, K.X., Huang, W.T., Luo, Z.B., Liang, H.Y., 2019. Magmatic response to slab tearing and resultant crustal evolution during scissor–like oblique continental collision: insights from Triassic mafic and felsic intrusions in the Qinling orogen, China. Lithos 344–345, 68–85.
Sajona, F.G., Bellon, H., Maury, R., Pubellier, M., Cotton, J., Rangin, C., 1994. Magmatic response to abrupt changes in geodynamic settings: Pliocene—Quaternary calc–alkaline and Nb–enriched lavas from Mindanao (Philippines). Tectonophysics 237 (1–2), 47–72.
Stampfli, G.M., Borel, G.D., 2002. A plate tectonic model for the Paleozoic and Mesozoic constrained by dynamic plate boundaries and restored synthetic oceanic isochrones. Earth Planet. Sci. Lett. 196 (1–2), 17–33.
Toksöz, M.N., Bird, P., 1977. Formation and Evolution of Marginal Basins and Continental Plateaus. Island Arcs, Deep Sea Trenches and Back–arc Basins. American Geophysical Union, Washington, pp. 379–393.
van de Zedde, D.M.A., Wortel, M.J.R., 2001. Shallow slab detachment as a transient source of heat at midlithospheric depths. Tectonics 20 (6), 868–882.
Vernon, R.H., Clarke, G.L., 2008. Principles of Metamorphic Petrology. Cambridge University Press, New York, p. 460.
Wang, Y.C., 2013. Geological Characteristics and Tectonic Significance of the Caledonian Syn– and Post–collisional Granites at the Conjunction of Qinling and Qilian Orogenic Belts. MS Dissertation. Chang'an University, Xi'an, pp. 1–86 (in Chinese with English abstract).
Wang, J., Zhang, H.F., Xu, W.C., Cai, H.M., 2008. Petrogenesis of granites from Dangchuan area in the western Qinling orogenic belt and its tectonic implications. Earth Sci. J. China Univ. Geosci. 33 (4), 474–486 (in Chinese with English abstract).
Wang, X.X., Wang, T., Zhang, C.L., 2013. Neoproterozoic, Paleozoic, and Mesozoic granitoid magmatism in the Qinling Orogen, China: constraints on orogenic process. J. Asian Earth Sci. 72, 129–151.
Wang, H., Wu, Y.B., Li, C.R., Zhao, T.Y., Qin, Z.W., Zhu, L.Q., Gao, S., Zheng, J.P., Zhou, L., Zhang, Y., Yang, S.H., 2014. Recycling of sediment into the mantle source of K–rich mafc rocks: Sr–Nd–Hf–O isotopic evidence from the Fushui complex in the Qinling orogeny. Contrib. Mineral. Petrol. 168 (4), 1–19.
Wang, L.J., Guo, J.H., Yim, C.Q., Peng, P., 2017. Petrogenesis of ca. 1.95 Ga meta–leucogranites from the Jining Complex in the Khondalite Belt, North China Craton: water–fluxed melting of metasedimentary rocks. Precambrian Res. 303, 355–371.
Wei, F.H., Pei, X.Z., Li, R.B., Li, Z.C., Pei, L., Gao, J.M., Wang, Y.C., Liu, C.J., Wu, K.S., Pei, Y.X., 2012. LA–ICP–MS zircon U–Pb dating of Early Paleozoic Huangmenchuan granodiorite in Tianshui area of Gansu Province and its tectonic significance. Geol. Bull. China 31 (9), 1496–1509 (in Chinese with English abstract).
Weinberg, R.F., Hasalová, P., 2015. Water fluxed melting of the continental crust: a review. Lithos 212–215, 158–188.
Whalen, J.B., Currie, K.L., Chappell, B.W., 1987. A–type granites: geochemical characteristics, discrimination and petrogenesis. Contrib. Mineral. Petrol. 95 (4), 407–419.
Wolf, M.B., Wyllie, P.J., 1994. Dehydration–melting of amphibolite at 10 kbar: the effects of temperature and time. Contrib. Mineral. Petrol. 115 (4), 369–383.

Wu, Y.B., Zheng, Y.F., 2013. Tectonic evolution of a composite collision orogen: an overview on the Qingling–Tongbai–Hong'an–Dabie–Sulu orogenic belt in Central China. Gondw. Res. 23 (4), 1402–1428.
Wu, F.Y., Liu, Z.C., Liu, X.C., Ji, W.Q., 2015. Himalayan leucogranite: petrogenesis and implications to orogenesis and plateau uplift. Acta Petrol. Sin. 31 (1), 1–36 (in Chinese with English abstract).
Wu, K., Ling, M.X., Hu, Y.B., Guo, J., Jiang, X.Y., Sun, S.J., Liang, H.Y., Liu, X., Sun, W.D., 2018. Melt–fluxed melting of the heterogeneously mixed lower arc crust: a case study from the Qinling Orogenic Belt, Central China. Geochem. Geophys. Geosyst. 19, 1767–1788.
Xu, T., Chen, Q.M., Guo, Q.M., Zhang, S.H., Mao, Y.L., Wang, Q., 2017. Age and geochemical features of the Early Devonian Xiangquan A–type syenogranites from Baoji area at the conjunction of Qinling and Qilian Orogen and their tectonic significance. Geol. Bull. China 36 (7), 1118–1128 (in Chinese with English abstract).
Yang, Y., 2017. Spatial–temporal Distribution and Sources of Granitoids in the Middle Qinling Orogenic Belt, Central China: Implications for the Nature of Deep Crustal Basement. PhD Thesis. Chinese Academy of Geological Sciences, Beijing, pp. 1–185 (in Chinese with English abstract).
Yi, J.K., Wang, Q., Zhu, D.C., Li, S.M., Liu, S.A., Wang, R., Zhang, L.L., Zhao, Z.D., 2018. Westward–younging high–Mg adakitic magmatism in central Tibet: record of a westward–migrating lithospheric foundering beneath the Lhasa–Qiangtang collision zone during the Late Cretaceous. Lithos 316–317, 92–103.
Yu, S., Li, S.Z., Zhao, S.J., Cao, H.H., Suo, Y.H., 2015. Long history of a Grenville orogen relic – the North Qinling terrane: evolution of the Qinling orogenic belt from Rodinia to Gondwana. Precambrian Res. 271, 98–117.
Yu, H., Zhang, H.F., Li, X.H., Zhang, J., Santosh, M., Yang, Y.H., Zhou, D.W., 2016. Tectonic evolution of the North Qinling Orogen from subduction to collision and exhumation: evidence from zircons in metamorphic rocks of the Qinling Group. Gondw. Res. 30, 65–78.
Zeng, L.S., Gao, L.E., Xie, K.J., Zeng, J.L., 2011. Mid–Eocene high Sr/Y granites in the Northern Himalayan Gneiss Domes: melting thickened lower continental crust. Earth Planet. Sci. Lett. 303 (3–4), 251–266.
Zhang, B.R., Gao, S., Zhang, H.F., Han, Y.W., 2002. Geochemistry of the Qinling Orogenic Belt. Science Press, Beijing, pp. 1–187 (in Chinese).
Zhang, H.F., Harris, N., Parrish, R., Kelley, S., Zhang, L., Rogers, N., Argles, T., King, J., 2004. Causes and consequences of protracted melting of the mid–crust exposed in the North Himalayan antiform. Earth Planet. Sci. Lett. 228 (1–2), 195–212.
Zhang, H.F., Zhang, B.R., Harris, N., Zhang, L., Chen, Y.L., Chen, N.S., Zhao, Z.D., 2006. U–Pb zircon SHRIMP ages, geochemical and Sr–Nd–Pb isotopic compositions of intrusive rocks from the Longshan–Tianshui area in the southeast corner of the Qilian orogenic belt, China: constraints on petrogenesis and tectonic affinity. J. Asian Earth Sci. 27 (6), 751–764.
Zhao, G.C., Wang, Y.J., Huang, B.C., Dong, Y.P., Li, S.Z., Zhang, G.W., Yu, S., 2018. Geological reconstructions of the East Asian blocks: from the breakup of Rodinia to the assembly of Pangea. Earth Sci. Rev. 186, 262–286.
Zheng, Y.F., 2012. Metamorphic chemical geodynamics in continental subduction zones. Chem. Geol. 328, 5–48.